Experimental characterization of the turbulent boundary layer over a porous trailing edge for noise abatement

Rubio Carpio, Alejandro; Merino Martínez, Roberto; Avallone, Francesco; Ragni, Daniele; Snellen, Mirjam; van der Zwaag, Sybrand

DOI
10.1016/j.jsv.2018.12.010

Publication date
2019

Document Version
Final published version

Published in
Journal of Sound and Vibration

Citation (APA)
Rubio Carpio, A., Merino Martínez, R., Avallone, F., Ragni, D., Snellen, M., & van der Zwaag, S. (2019). Experimental characterization of the turbulent boundary layer over a porous trailing edge for noise abatement. *Journal of Sound and Vibration*, *443*, 537-558. https://doi.org/10.1016/j.jsv.2018.12.010

Journal of Sound and Vibration 443 (2019) 537–558

Contents lists available at ScienceDirect

Journal of Sound and Vibration

journal homepage: www.elsevier.com/locate/jsvi

Experimental characterization of the turbulent boundary layer over a porous trailing edge for noise abatement

Alejandro Rubio Carpio *, Roberto Merino Martínez, Francesco Avallone, Daniele Ragni, Mirjam Snellen, Sybrand van der Zwaag

Faculty of Aerospace, Delft University of Technology, Delft 2629HS, The Netherlands

ARTICLE INFO

Article history:
Received 15 May 2018
Revised 6 December 2018
Accepted 7 December 2018
Available online 10 December 2018
Handling Editor: R.E. Musafir

Keywords:
Trailing edge noise
Noise reduction
Porous materials
Metal foams

ABSTRACT

The hydrodynamic and acoustic fields for a NACA 0018 with solid and porous trailing edge inserts are investigated. The porous inserts, covering 20% of the chord, are manufactured with metal foams with cell diameters of 450 and 800 μm and permeability values of 6×10^{-10} and 2.7×10^{-9} m^2. The experiments are performed at a chord-based Reynolds number of 2.63×10^5 and an angle of attack of 0°. The porous trailing edge with higher permeability provides up to 11 dB noise attenuation with respect to the solid case for frequencies below a cross-over Strouhal number $St = 0.26$. Lower noise abatement (up to 7 dB) takes place below $St = 0.3$ for the insert with lower permeability. Conversely, noise increase with respect to the solid case is measured above the previously defined St value. A decrease in turbulence intensity is reported (up to 3% of the free-stream velocity), with lower intensity being measured for the insert with lower permeability. It is also observed that the permeability of the insert is linked to the increase of the anisotropy of highly energetic turbulent motions, being stretched in the streamwise direction, and the reduction of the eddy convection velocity (up to 20% with respect to the baseline case). In view of the results, the reduction of the velocity fluctuations is proposed as one of the mechanisms for low frequency noise abatement, being more relevant for the metal foam insert with lower permeability.

1. Introduction

Broadband trailing edge noise is generated by turbulence structures convecting over the trailing edge of an airfoil [1]. This source of noise is relevant for the wind turbine industry since it represents the main contributor to the overall noise produced by modern wind turbines [2]. For this reason, passive and active noise reduction techniques such as the boundary layer injection/suction [3–5], the aeroacoustic optimization of the airfoil shape [6,7], the use of trailing edge serrations [8–10], finlets [11] or trailing edge brushes [12,13] have been considered. Among others, the usage of permeable trailing edges has been shown to be effective in reducing noise, but the relation between the pore characteristics and the degree of noise reduction has not yet been studied in detail, nor has the responsible mechanism been identified. For this reason, noise reduction due to the presence of permeable trailing edges is analysed in this manuscript.

The idea of using porous materials for noise attenuation dates back to the investigation of Graham [14] on the silent flight of the owl in the 30s. Since then, porous materials have been applied to mitigate noise generated at the leading edge [15] and the trailing edge flap [16]. Recently, novel applications of porous materials in blunt bodies, such as cylinders [17] or flat plates

* Corresponding author.
E-mail address: a.rubiocarpio@tudelft.nl (A.R. Carpio).

https://doi.org/10.1016/j.jsv.2018.12.010
0022-460X/

[18], or their use between serrations cut into the airfoil (poro-serrated trailing edge) [19,20] demonstrated their capability to break down vortex shedding, hence reducing the associated acoustic tone. Similarly to the poro-serrated edges, the application of combs between serrations [21] overcame the baseline serration broadband noise attenuation performance up to 2 dB; the additional noise abatement was attributed to an improved capability to distribute the noise sources along the edge of the serrations, thus promoting destructive interference among them [22].

Another approach previously addressed in the literature was the partial or total manufacture of airfoils with porous materials; in comparison with the application of trailing edge add-ons, this strategy represents a favored solution from a structural integrity point of view, specially relevant for wind turbines at high loading. For instance, Geyer et al. [23,24] carried acoustic measurements on fully porous SD7003 airfoils showing trailing edge noise reduction up to 10 dB with respect to the baseline solid airfoil. It was also found that the frequency range at which noise reduction was measured depends on specific foam properties such as porosity and resistivity. The fully porous airfoil did show noise attenuation benefits, but this solution also caused a decrease of up to 80% in lift, compared to the baseline airfoil, and up to ten times more drag. To mitigate the loss in aerodynamic performance, Geyer and Sarradj [25] restricted the use of porous materials to the trailing edge. They found far-field noise abatement up to 8 dB even with a porous extent limited to the last 5% of the chord. With that configuration, only a 6% increase in drag was reported while the decrease in lift was negligible.

Further acoustic measurements on partially porous airfoils were carried out by Herr et al. [26]. Different permeable materials were tested on a DLRF16 airfoil trailing edge with a porous insert length equal to 10% of the chord. They reported noise reduction with respect to the solid case at lower frequencies (up to $f = 10$ kHz depending on the porous material) and noise increase above this frequency. The noise increase, attributed to a surface roughness contribution [24], was linked to the pore size. Larger noise abatement at lower frequencies was obtained using materials with higher permeability. However, no boundary layer data were reported in this investigation.

Despite the extensive far-field noise datasets, published data on the hydrodynamic field over the porous trailing edge are limited. This is due to the fact that it is difficult to accurately measure the flow within the material and in the near-wall regions. Additionally, numerical computations are expensive and the results depend on the closure model that accounts for flow through porous media [27].

Previous studies [18,24,25] show a high dependence of the mean flow field and turbulence intensity above the insert on the characteristics of the porous material. Nevertheless, the effect of the porous treatment on the turbulence intensity remains unclear: it is shown to decrease [18] or increase [25] with respect to the solid case for porous materials with similar properties. Such behavior might be indicative of a strong dependence not only on the material but also on set-up characteristics such as the model, length of porous insert or angle of attack. Furthermore, measurements on completely [24] and partially [25] porous airfoils showed changes in the boundary layer topology, i.e. an increase in the boundary layer and displacement thickness with respect to the reference case. This modification suggests that classic theory of noise generation at solid edges [28] is not adequate for porous inserts.

Given the inconclusive aspects of noise attenuation using permeable materials encountered in previous literature, the current investigation presents a study where the boundary layer above porous trailing edge inserts and their noise scattering are characterized. Measurements are carried out on a NACA 0018 airfoil at a chord-based Reynolds number of 2.63×10^5 and no incidence. Time-resolved Particle Image Velocimetry (PIV) is employed to acquire the 2D-2C velocity field at the midspan plane above the two different open-cell metal foam inserts, as well as a reference (solid) one. Relevant quantities for trailing edge noise generation on solid edges [29,30], such as root-mean-square (r.m.s.) velocity, integral length scales, spectra of the velocity fluctuations and convection velocity, are evaluated close to the trailing edge to analyse whether they can be linked to the far-field noise, measured with a microphone array. The metal foams are characterized in terms of permeability and porosity, and a detailed description of their topology is also included.

The manuscript is organized as follows. First, the measurement set-up, the metal foam characterization procedure and properties, the data reduction procedure, and the acoustic phased array and PIV arrangement are presented in Section 2. Then, far-field noise measurements, mean flow field, statistics and velocity spectra are discussed in Section 3. Finally, in Section 4 a summary of the findings is reported.

2. Experimental set-up

2.1. Wind tunnel facility and model

The experiments are performed in the anechoic vertical open-jet wind tunnel (AV-Tunnel) at Delft University of Technology. It has a contraction ratio of 15:1 and it can be operated at a free-stream velocity up to 45 m/s. The rectangular test section is $40 \times 70\ \text{cm}^2$. The turbulence intensity is below 0.1% for the entire range of operative velocities. The free-stream velocity distribution across the test section is uniform within 0.5%. A NACA 0018 airfoil (Fig. 1(a)), with chord c and span L lengths of 0.2 m and 0.4 m (span-chord ratio $L/c = 2$), is installed between two 1.2 m long side plates to guarantee two-dimensional flow (Fig. 3(a)). The airfoil, located 50 cm away from the contraction exit, is manufactured using Computer Numerical Control Machining (surface roughness: 0.05 mm) from a solid aluminium plate. It has exchangeable trailing edges to allow the testing of different porous materials, as well as the reference configuration. The porous trailing edge inserts, manufactured using Electrical Discharge Machining, cover the last 20% (0.04 m) of the chord (Fig. 1 (b)) to guarantee relevant changes in the flow field and acoustic emissions with respect to the solid case. Pictures of the two types of inserts used in the experiments, with cell diameter

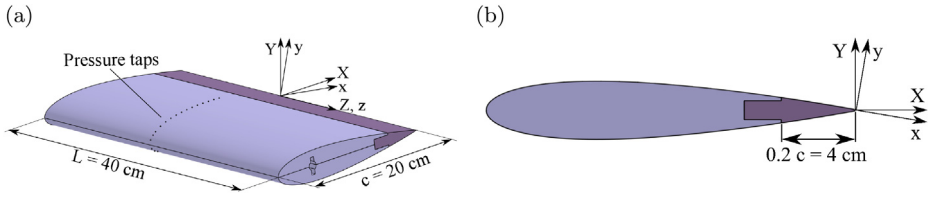

Fig. 1. Sketch of the NACA 0018 airfoil with porous insert. The aluminum body is represented in pale purple while the metal foam insert appears in dark purple. (a) General view. (b) Side view. (For interpretation of the references to colour in this figure legend, the reader is referred to the Web version of this article.)

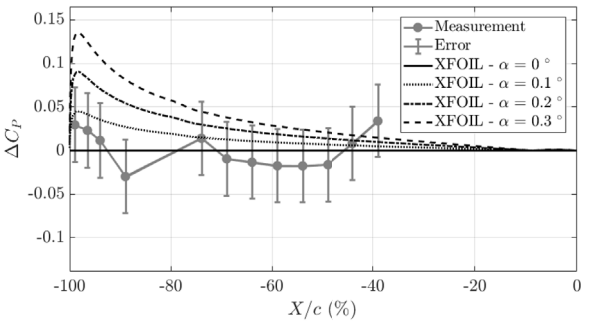

Fig. 2. Differential pressure coefficient ΔC_P distribution along the chord of the airfoil.

of $d_c = 450$ μm and $d_c = 800$ μm are respectively presented in Fig. 3(b) and (c). The current experimental set-up is employed due to the availability of extensive aerodynamic [31–33] and acoustic [34,35] validation data regarding wind energy research.

Two coordinate systems, detailed in Fig. 1(a) and (b), are used in the present manuscript. Both coordinate systems have the origin at the intersection between the trailing edge and the midspan plane of the airfoil. The $X - Y - Z$ system, used to describe the experimental set-up, has the X and Z-axis aligned with the chord and the trailing edge of the airfoil. The $x - y - z$ coordinate system, used for the boundary layer analysis, is rotated with respect to the previously defined streamwise-vertical plane $X - Y$ so that the x and y directions are parallel and normal to the top surface of the trailing edge insert, respectively.

In order to assess the angle of attack α, static pressure measurements are obtained through 15 differential pressure *Honeywell* TruStability transducers (range: −2.5–2.5 kPa; accuracy: 12.5 Pa). Data are recorded at a sampling frequency of 100 Hz for 10 s. The pressure transducers are connected to 30 pressure taps of 0.4 mm diameter, located within chordwise positions $-0.99 \leq X/c \leq -0.34$, and equally distributed between the suction and the pressure sides. The taps are tilted 15° with respect to the midspan plane of the airfoil ($Z = 0$) to avoid interference between the wake of the cavities and sensors located downstream. The angle of attack is evaluated by comparing the measured surface pressure distribution with the one given by the vortex-panel method XFOIL [36], as shown in Fig. 2. Data are presented in terms of the differential pressure coefficient ΔC_P, defined as:

$$\Delta C_P = \frac{\Delta P}{\frac{1}{2}\rho_\infty U_\infty^2} \tag{1}$$

as a function of X/c. Note that the differential static pressure ΔP is precisely the quantity measured by the sensors, and that measurements performed at $X/c = -84$, -79 and -34% are not shown since the orifices were covered by the trip or blocked by dust during the experiments. For the sake of clarity, static pressure distributions corresponding to angles of attack with values up to 0.3° are also shown. Measured data agree with the $\alpha = 0°$ curve retrieved from XFOIL within the uncertainty range.

Turbulent boundary-layer transition is forced at $X/c = -0.8$ at both suction and pressure sides with carborundum particles of 0.84 mm diameter randomly distributed on a 10 mm tape strip. A stethoscope probe [31,37,38] is employed to confirm that the boundary layer flow downstream the strip location is turbulent; a detailed description of the system employed in the present experiment is presented in Lentink et al. [39]. The experiments are performed at a chord-based Reynolds numbers of 2.63×10^5, corresponding to a free-stream velocity $U_\infty = 20$ m/s, and an angle of attack of 0°.

2.2. Porous materials

Porous inserts are fabricated with two different types of *Alantum* NiCrAl open-cell metal foams. Both foams have been manufactured by electrodeposition of pure Ni on a polyurethane foam and subsequent coating with high-alloyed powder [40]. Thus, they share a homogeneous microstructure consisting of the three-dimensional repetition of a dodecahedron-shaped cell, as seen in the microscopy images presented in Fig. 4. Additionally, it has been verified that the cell diameter d_c, defined in the microscopy pictures, is in agreement with the nominal d_c (450 and 800 μm) provided by the manufacturer *Alantum*.

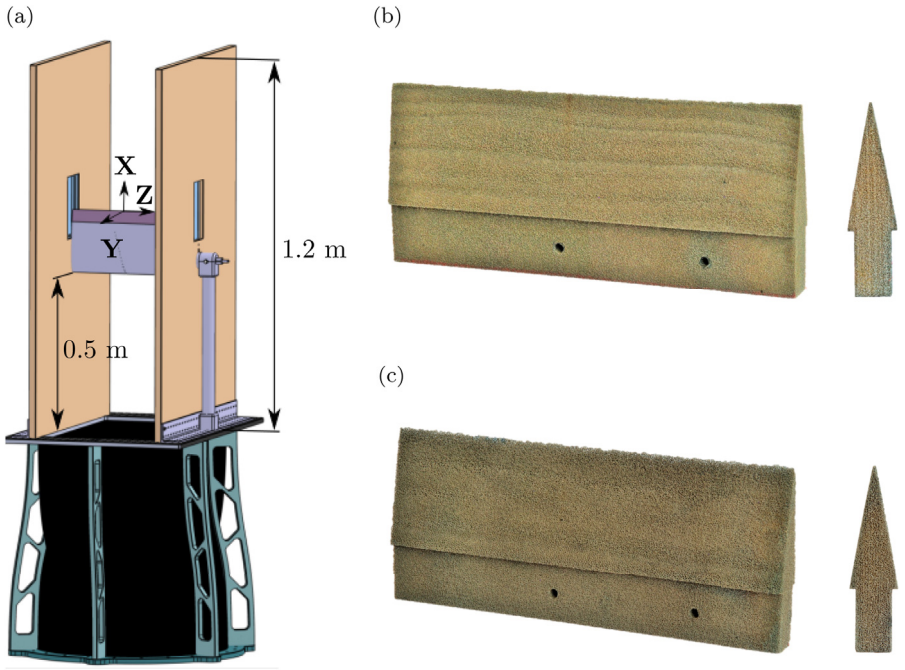

Fig. 3. (a) Sketch of the test section with the NACA 0018 airfoil installed between two side plates, depicted in brown, with optical access. (b) Pictures of the $d_c = 450$ µm metal foam insert. (c) Pictures of the $d_c = 800$ µm metal foam insert. (For interpretation of the references to colour in this figure legend, the reader is referred to the Web version of this article.)

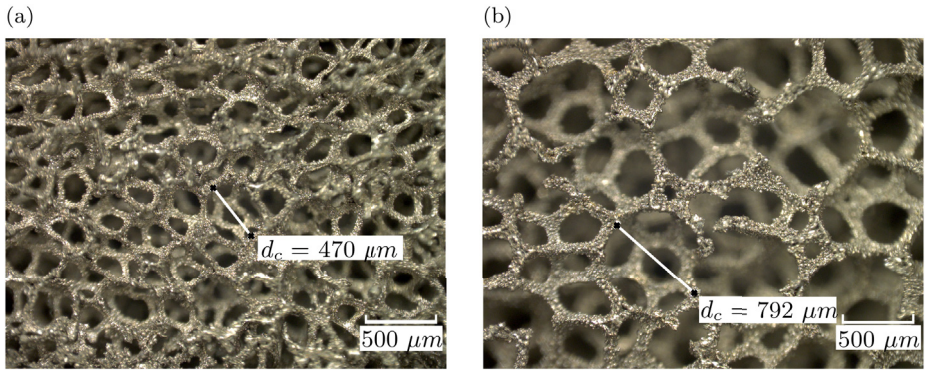

Fig. 4. 2D microscopy images of the 2 metal foams used in the experiments. (a) $d_c = 450$ µm. (b) $d_c = 800$ µm. Total field of view in the images is 3.05×2.28 mm^2. Resolution: 525 px/mm.

2.2.1. Porosity

The porosity of the metal foam σ is defined as:

$$\sigma = 1 - \frac{\rho_p}{\rho_b} \tag{2}$$

where ρ_p and ρ_b are respectively the density of the foam and the base alloy (NiCrAl). The density of the porous foam ρ_p is calculated as the ratio between the weight and the volume of $10 \times 10 \times 5$ mm^3 samples. The samples are weighted using a *Mettler* Toledo AB204S analytical balance. In order to retrieve the density of the base alloy ρ_b, the approximate composition is obtained by energy-dispersive X-ray spectroscopy (EDS). The EDS analysis is carried out employing a *Jeol* JSM-7500F Field Emission Scanning Electron Microscope on the same samples used to calculate ρ_p. The measured values for the porosity are presented in Table 1. It is verified that the porosity of the $d_c = 450$ µm and $d_c = 800$ µm metal foams is respectively 89.3 and 91.7%, in agreement with nominal data provided by the manufacturer (85 and 90%).

Table 1
Measured metal foam properties. Values in parenthesis refer to values provided by the manufacturer.

d_c (μm)	σ (%)	R (Ns/m^4)	K (m^2)	C (m^{-1})
(450)	89.3	29850	6×10^{-10}	9758
(800)	91.7	6728	27×10^{-10}	2613

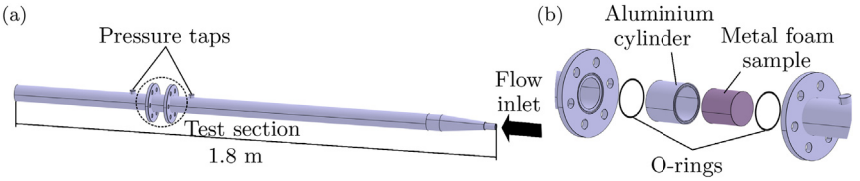

Fig. 5. (a) Sketch of the rig used to characterize the permeability/resistivity of the metal foams used during the experiments. (b) Detail of the test section.

2.2.2. Permeability

The static pressure drop Δp across a homogeneous sample of permeable material with thickness t is described by the Hazen-Dupuit-Darcy equation [41].

$$\frac{\Delta p}{t} = \frac{\mu}{K} v_d + \rho C v_d^2 \tag{3}$$

where ρ is the fluid density, μ is the dynamic viscosity, v_d is the Darcian velocity (defined as the ratio between the volumetric flow rate and the cross-section area of the sample) and K and C are the permeability and the form coefficient, accounting for pressure loss due to viscous and inertial effects respectively. These two properties are obtained by least-squares fitting of Eq. (3) to 20 pressure drop data, measured for Darcian velocities ranging between 0 and 2.5 m/s.

The permeability measurements are carried out using the experimental rig shown in Fig. 5, specifically built for this purpose. The rig, supplied by air at 10 bar, allows to measure Δp between two pressure taps placed 5 cm upstream and downstream of the test section. The pressure taps are connected to a Mensor 2101 differential pressure sensor (range: −1.2–15 kPa; accuracy: 2 Pa). The volumetric flow rate is controlled using an *Aventics* pressure regulator and measured by a *TSI* 4040 volumetric flow meter (range: 0–2.5 m/s; accuracy: 2% of reading) located upstream the pipe.

The test section consists of an aluminum cylinder, into which 55 mm diameter metal foam disks are inserted. Previous studies [42,43] showed that the permeability/drag coefficient measured on thin samples are biased due to the prevalence of entrance/exit effects on the measured pressure drop. To study the effect of the sample thickness, t, on K and C, samples with t ranging from 10 mm to 60 mm are tested. It is verified that values of K and C obtained on foam samples with 50 and 60 mm thickness are approximately equal, i.e. entrance/exit effects are negligible. These values, reported in Table 1, are in agreement with those published in previous literature [44,45]. As expected, results show that the metal foam with larger pore size is more permeable.

On previous research on trailing edge noise reduction using porous media [46,47], the air flow resistivity $R = \Delta p/(t\, v_d)$ was used to characterize the flow-metal foam interaction. This metal foam property, estimated in the present manuscript as $R = \mu/K$, is also presented in Table 1 for comparison.

2.3. Scattered noise and related boundary layer quantities

The hydrodynamic quantities driving the generation of broadband trailing edge noise on a solid airfoil, which are analysed in the remaining of the manuscript, are described in this section. Under the assumptions of large span-to-chord ratio ($L/c > 1$) and frozen turbulence [48], Amiet's analytical model [49] relates the far-field acoustic pressure to wall-pressure fluctuations close to the trailing edge for acoustic wavelengths sufficiently smaller than the chord. The general expression for the power spectral density of the far-field acoustic pressure $S_{pp}(X, Y, Z, \omega)$ for an observer placed at the midspan plane of the airfoil ($Z = 0$) is given by Refs. [49,50].

$$S_{pp}(X, Y, Z = 0, \omega) = \left(\frac{\omega c Y}{4\pi c_0 \sigma^2} \right)^2 \frac{L}{2} |\mathscr{L}|^2 \phi_p \Lambda_{p|z} \tag{4}$$

where $\sigma = X^2 + \beta^2 Y^2$ is the flow-corrected distance between observer and trailing edge, $\beta = \sqrt{1 - (U_\infty/c_0)^2}$ is the Prandtl-Glauert factor and $\mathscr{L}$ is the acoustically weighted lift function.[1] In Eq. (4), the product of the power spectral density ϕ_p and the spanwise coherence length $\Lambda_{p|z}$ of the surface pressure fluctuations, evaluated at the trailing edge, acts as the source of the

[1] The reader is referred to the original publication of Amiet [49–51] for its detailed description.

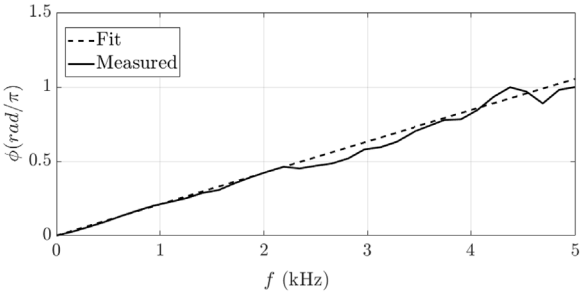

Fig. 6. Variation of the phase of the cross-spectra $\phi(x+\xi_x,y,f)$ with frequency for separation length $\xi_x = 1.5$ mm at the reference point $(x/c = -0.02, y/\delta_{99} = 0.7)$ above the solid insert.

far-field acoustic scattering. Using the TNO-Blake model [29,52], this term can be linked to boundary layer kinematic quantities. In this formulation, valid for solid airfoils at low angles of attack [30,53], the source term is computed as

$$\phi_p \Lambda_{p|z} = 4\pi\rho^2 \int_0^{\delta_{99}} \Lambda_{vv|y}(\mathbf{x}) U_c(\mathbf{x}) \Phi_{vv}(\mathbf{x},f) \left(\frac{\partial U(\mathbf{x})}{\partial y}\right)^2 \frac{\overline{v^2}(\mathbf{x})}{U_c(\mathbf{x})^2} e^{-2|k|y} \mathrm{d}y \tag{5}$$

where $\mathbf{x} = (x,y)$ defines the position of the reference point, $\Phi_{vv}(\mathbf{x},f)$ is the power spectral density of the wall-normal velocity fluctuations, $\Lambda_{vv|y}(\mathbf{x})$ is the wall-normal correlation length of the wall-normal velocity fluctuations and $U_c(\mathbf{x})$ is the streamwise convection velocity of the turbulent structures. In the reminder of the study, these quantities are calculated above the permeable and solid inserts, where differences might explain changes in broadband trailing edge noise emission.

The power spectral density of the velocity fluctuations $\Phi_{ii}(\mathbf{x},f)$ is defined as:

$$\Phi_{ii}(\mathbf{x},f) = \int_{-\infty}^{\infty} R_i(\mathbf{x},\tau) e^{-2\pi \mathrm{j} f\tau} \mathrm{d}\tau \tag{6}$$

where the auto-correlation function $R_i (i = [u,v])$ is defined as:

$$R_u(\mathbf{x},\tau) = \frac{\overline{u(\mathbf{x},t)u(\mathbf{x},t+\tau)}}{\overline{u^2(\mathbf{x})}} \tag{7a}$$

$$R_v(\mathbf{x},\tau) = \frac{\overline{v(\mathbf{x},t)v(\mathbf{x},t+\tau)}}{\overline{v^2(\mathbf{x})}} \tag{7b}$$

with τ being the time delay. To calculate $\Phi_{ii}(\mathbf{x},f)$, Hanning windows of 128 elements and 50% overlapping were used, thus resulting in a frequency resolution of 78 Hz. Agreement between the energy content of the signal in the time and frequency domain (Parseval's theorem [54]) is assessed.

Another important noise production related parameter, the length scale $\Lambda_{vv|y}(\mathbf{x})$ is linked to the wall-normal length of turbulence structures. This quantity, calculated on the uncorrelated data set, is defined as:

$$\Lambda_{vv|y}(\mathbf{x}) = \int_0^{\infty} R_v(\mathbf{x}+\boldsymbol{\xi},\tau=0)\mathrm{d}y = \int_0^{\infty} \frac{\overline{v(x,y,t)v(x,y+\xi_y,t)}}{\sqrt{\overline{v^2(x,y)}\overline{v^2(x,y+\xi_y)}}} \mathrm{d}y \tag{8}$$

where $\boldsymbol{\xi} = (\xi_x,\xi_y)$ refers to the separation vector (note that $\xi_x = 0$ since only the wall-normal length scale is considered). Convergence of the $\Lambda_{vv|y}(\mathbf{x})$ values within the number of acquired uncorrelated samples is verified. The integration is performed within the range $y \in \left[0.2\delta_{99}, 1.7\delta_{99}\right]$ similarly to Kamruzzaman et al. [55] and Arce León et al. [35].

The streamwise convection velocity $U_c(\mathbf{x})$ is calculated following the method proposed by Romano [56]:

$$U_c(\mathbf{x}) = 2\pi\xi_x \frac{\partial f}{\partial \phi(x+\xi_x,y,f)} \tag{9}$$

where $\phi(x+\xi_x,y,f)$ refers to the phase of the cross-spectra of the wall-parallel fluctuations u between two points separated by a wall-parallel distance ξ_x.

An example of the variation of $\phi(x+\xi_x,y,f)$ with frequency for $\xi_x = 1.5$ mm is shown in Fig. 6. The measured slope $d\phi/df(x+\xi_x,y,f)$ is practically constant within the low frequency range. Nevertheless, deviation from linearity takes place at higher frequencies due to loss of correlation. In order to avoid mislead on the calculation of $U_c(\mathbf{x})$, measured $\phi(x+\xi_x,y,f)$ are fitted with a line considering data up to cut-off frequency $f_{co} = 500$ Hz, similarly to Avallone et al. [10]. Dependence of the calculated convection velocity on f_{co} is also studied, being assessed that fitting data up to $f_{co} = 1$ kHz yields similar results. Due to the employed measurement technique, a wide range of different separation lengths ξ_x is available. The ultimate $U_c(\mathbf{x})$ value is estimated as the mean of the ensemble of $U_c(\mathbf{x})$ values corresponding to different ξ_x.

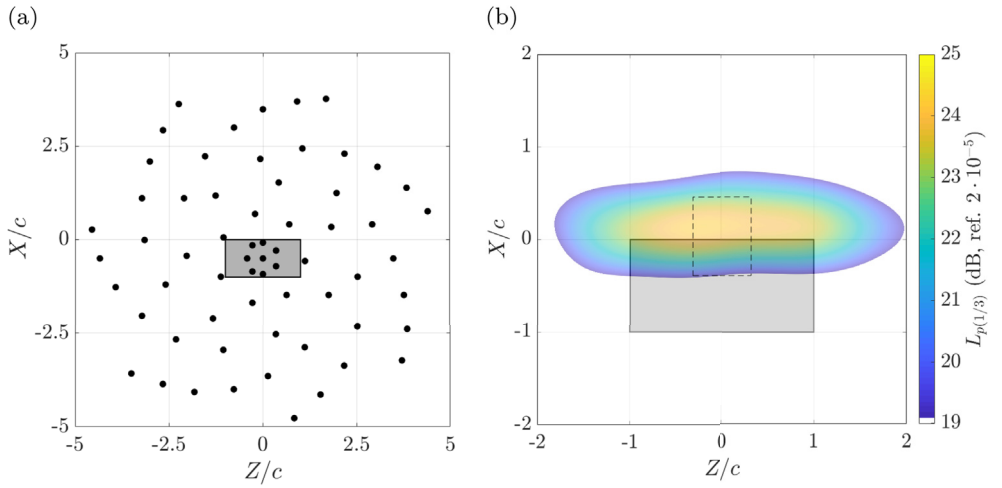

Fig. 7. (a) Distribution of phased microphones within the array. Coordinates are shown in the airfoil system $X - Y - Z$. The shaded area in grey represents the airfoil position with the flow direction in the positive X direction. (b) Source plot of the reference case for the 1/3 octave band with center frequency at $f = 1.6$ kHz. The projection of the airfoil in the $X - Z$ plane is depicted. The integration area is depicted as a dashed box.

2.4. Acoustic phased array set-up

A phased microphone array consisting of 64 G.R A.S. 40 PH free-field microphones (frequency response: ±1 dB; frequency range: 10 Hz to 20 kHz; max. output: 135 dB ref. 2×10^{-5} Pa; nominal phase spreading: ±3°) with integrated CCP pre-amplifiers is employed for measuring the far-field noise generated at the trailing edge. The distribution of the microphones is an adapted Underbrink design [57] with 7 spiral arms of 9 microphones each, and an additional microphone located at the center of the array (Fig. 7(a)). The diameter of the array D_a is 2 m and the distance from the array plane to the airfoil trailing edge $d_{\text{a-TE}}$ is 1.43 m. The center of the array is approximately aligned with the center of the airfoil trailing edge.

A sampling frequency of 50 kHz and a recording time T of 60 s are used for each measurement. The acoustic data is separated in time blocks of 8192 samples ($\Delta t = 164$ ms) for each Fourier transform and windowed using a Hanning weighting function with 50% data overlap, thus providing a frequency resolution of 6.1 Hz. The cross-spectral matrix (CSM) of the measured acoustic pressure is obtained by averaging the Fourier-transformed sample blocks over time. In previous studies [58] with a similar experimental set-up, the source power was retrieved within an accuracy of 1 dB. Beamforming is performed on a square grid ranging between $-2 < X/c < 2$ and $-2 < Z/c < 2$ and distance between grid points of 1 cm. The minimum distance at which the array can resolve two sources is given by the Rayleigh criterion [59,60] as

$$R \simeq d_{\text{a-TE}} \tan\left(\frac{1.22 c_0}{f D_{\text{a}}}\right) \tag{10}$$

where c_0 is the speed of sound. For the highest measured frequency shown in the present investigation ($f = 3$ kHz), Eq. (10) yields a minimum distance of $R = 10$ cm. Hence, the space between grid points is 10 times smaller than the maximum resolution of the array. Conventional frequency domain beamforming [61] is applied to the acoustic data. The minimum frequency for the acoustic spectra is 500 Hz. In order to minimize the effect of neighbouring sources of noise, integration of the source map in the range $-0.33 < Z/c < 0.33$ and $-0.4 < X/c < 0.4$ (dashed box in Fig. 7(b)) is performed [35]. This method has been shown to provide with very satisfactory results for trailing edge noise data obtained through simulations [62] and experiments [63,64].

2.5. High speed Particle Image Velocimetry

Two-dimensional two-component (2D2C) PIV measurements are performed in the wall-parallel/wall-normal plane ($x - y$) at the midspan of the airfoil. The experimental set-up is depicted in Fig. 8(a).

Seeding is produced by a *SAFEX* Twin-Fog Double Power fog generator using a glycol-based solution with mean droplet diameter of 1 μm. Illumination is provided by laser pulses generated by a *Quantronix* Darwin Duo 527-80-M double cavity Nd:YLF system (laser wavelength: 527 nm; energy: 30 mJ/pulse). Laser optics are used to turn the laser beam into a laser sheet of approximately 1 mm thickness.

Images are recorded using a *Photron* Fastcam SA-1 CMOS camera (1024×1024 pixel^2, 12 bit, pixel size 20 μm), placed at 25 cm from the measurement plane. The camera is equipped with a *Nikon* NIKKOR 105 mm focal distance macro-objective set at $f_{\#} = 5.6$. The image acquisition and the illumination are triggered synchronously using a *LaVision* high speed controller. Time-resolved data is acquired at a sampling frequency of 5 kHz (5457 image pairs). The sensor of the camera is cropped to 1024×512 pixels. The final field of view (FOV), shown in Fig. 8(b), is of $0.2c \times 0.1c$ (40×20 mm^2) with a digital resolution of

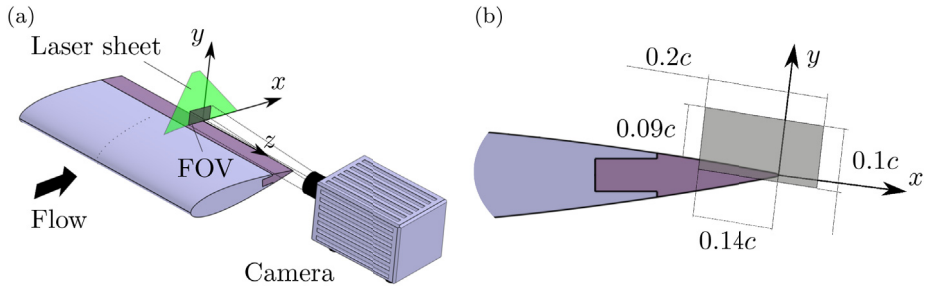

Fig. 8. (a) Sketch of the PIV set-up. (b) Detail of the FOV and coordinate system.

Table 2
PIV acquisition parameters.

Parameter	Quantity
Camera	*Photron* Fastcam SA1.1
Acquisition frequency	10 kHz
Separation time between camera exposures	100 μs
Acquisition sensor	512 × 1024 px^2
Field of view (FOV)	20 × 40 mm^2
Digital resolution	25 px/mm
Magnification factor	0.51
Interrogation window	24 × 24 px^2
Overlap factor	75%
Vectors per velocity field	88 × 172
Vector spacing	0.24 × 0.24 mm^2
Free-stream pixel displacement	40 px

approximately 25 px/mm. The measured area above the trailing edge is confined between $-0.14 \leq x/c \leq 0$ in the wall-parallel direction and $0 \leq y/c \leq 0.09$ in the wall-normal direction. Due to the presence of laser reflections at the surface discontinuity, data measured at $-0.02 < x/c \leq 0$ are not reported. The separation time between camera exposures is set at 100 μs allowing for reshuffling of the image pairs into a continuous sequence (10914 images) with an effective sampling frequency of $f_s = 10$ kHz.

Processing of the images is carried out using *LaVision* DaVis 8.4 software. A multi-pass cross-correlation algorithm [65] with window deformation [66] is applied to the sequence of images resulting in 10913 vector fields. The final interrogation window size is 24 × 24 pixel^2 with 75% of overlapping, yielding a final spatial resolution of 0.94 mm and a vector spacing of 0.24 mm. Finally, spurious vectors are discarded by applying a universal outlier detector [67] and are replaced by interpolation based on adjacent data. The main characteristics of the camera and the acquisition parameters are summarized in Table 2.

2.5.1. Uncorrelated dataset

The mean and turbulent flow fields are obtained by under-sampling the correlated dataset with a frequency $f_{us} = 333$ Hz, thus yielding a data-set of 364 PIV snapshots. The under-sampling frequency is chosen by analysing the auto-correlation function R_i of the wall-parallel u and wall-normal v velocity fluctuations, defined in Eq. (7a) and (7b), at the point of maximum intensity of the velocity fluctuations ($x/c = -0.02, y/\delta_{99} = 0.5$) above the solid insert.

As seen in Fig. 9(a), the autocorrelation function for both wall-normal and wall-parallel velocity fluctuations is negligible at a time delay $\tau = 3$ ms, corresponding to the previously defined under-sampling rate $f_{us} = 1/\tau$. The cumulative mobile mean of the mean (U, V) and r.m.s $(\sqrt{\overline{u^2}}, \sqrt{\overline{v^2}})$ velocity components, presented in Fig. 9(b), is used to assess convergence to an asymptotic value within a reduced data-set with n_s samples.

2.5.2. Uncertainty analysis

The estimation of the PIV uncertainty is carried out quantifying the random and systematic (bias) errors. The random error is due to uncertainty on the cross-correlation analysis, which cannot accurately represent the stochastic nature of turbulence. The cross-correlation error is associated to the sub-pixel interpolation (3-points Gaussian fit). This error is estimated at 0.1 pixel based on the study of Westerweel [68]. The effect of turbulence on the convergence of statistic quantities, which depends on the total number of uncorrelated samples ($N_s = 364$), is also taken into account.

The most important systematic errors are typically peak-locking, particle slip, calibration errors and lack of spatial resolution. Peak-locking consists of a bias of the correlation peak position towards integer displacement. In order to minimize this source of error, the particle image is kept larger than 2 pixels, as suggested in Raffel et al. [69]. The histogram of the round-off residual of the particle displacement $\Delta x_i - [\Delta x_i]$, where $[\cdot]$ refers to the round function, is depicted in Fig. 10(a); it shows that no bias towards integer values is present on the instantaneous PIV snapshots. In Fig. 10(b), the cumulative sum of the measured decimal

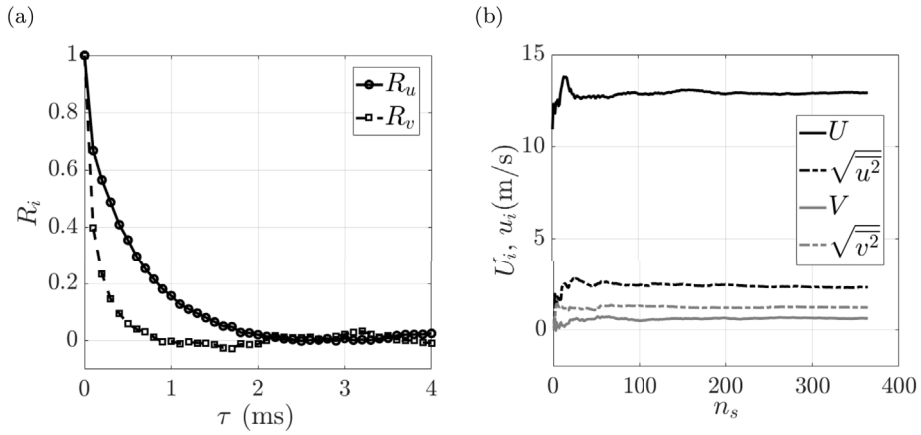

Fig. 9. (a) Auto-correlation function of the wall-parallel and wall-normal velocity fluctuations at $(x/c = -0.02, y/\delta_{99} = 0.5)$. (b) Convergence of mean and r.m.s. wall-parallel and wall-normal velocity with increasing number of samples n_s within the reduced data-set.

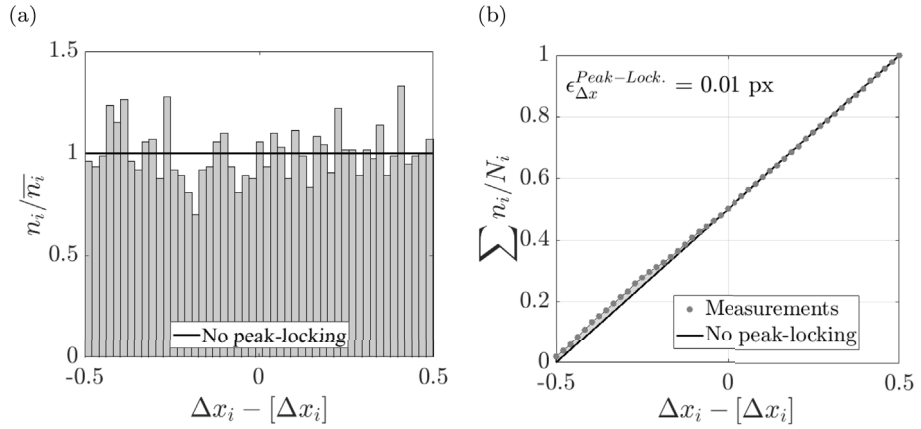

Fig. 10. (a) Histogram binning $\Delta x_i - [\Delta x_i]$. (b) Cumulative sum of $\Delta x_i - [\Delta x_i]$ values in each bin. The grey area between the black line and the grey circle markers gives an estimation of peak-locking error. n_i and N_i refer to the number of values inside each bin and the total number of vectors within an instantaneous PIV snapshot, respectively.

particle displacement, used to quantify this source of error, is shown. The error due to peak-locking is found to be always around one order of magnitude smaller than the cross-correlation error, hence it is considered negligible.

Another source of systematic error is the particle slip, caused by the lag between the tracer and the flow subject to measurement. The particle slip error [70] is calculated as $U_{\text{slip}} = \tau_{\text{slip}} a_p$, where the particle acceleration a_p is obtained through the material derivative of the velocity field. The response time associated to the tracer particle $\tau_{\text{slip}} = 0.5$ µs is satisfactory for the average particle acceleration found in the boundary layer (2900 m/s^2), yielding a final U_{slip} of 0.01% of the free-stream velocity.

Spatial calibration of the camera is applied using a three-dimensional known target, with a positioning error of ±0.5 mm. To account for any optical distortion, images are mapped using a third order polynomial fit (r.m.s of fit: 0.26 pixel) which allows mapping of the physical space into the sensor one.

Using a linear propagation approach [71], the uncertainty on the mean and r.m.s. velocity have respectively upper bound values of $0.02U_\infty$ and $0.04\sqrt{u^2}$, found at the point of maximum intensity of the velocity fluctuations defined in section 2.5.1. These values are verified using the error quantification method introduced by Wieneke [72]. The latter gives an uncertainty on the mean quantities of $0.01U_\infty$ and on the r.m.s. quantities of $0.03\sqrt{u^2}$, considering a 95% confidence interval.

Finally, the error in the measurement of flow structures size due to the finite dimension of the interrogation window is quantified using the method proposed by Schrijer et al. [73]. Due to the multi-pass iterative cross-correlation algorithm, flow structures up to $0.21\delta_{99}^{\min}$ can be measured with an accuracy within 10%, with $\delta_{99}^{\min}$ the minimum boundary layer thickness reported in this manuscript.

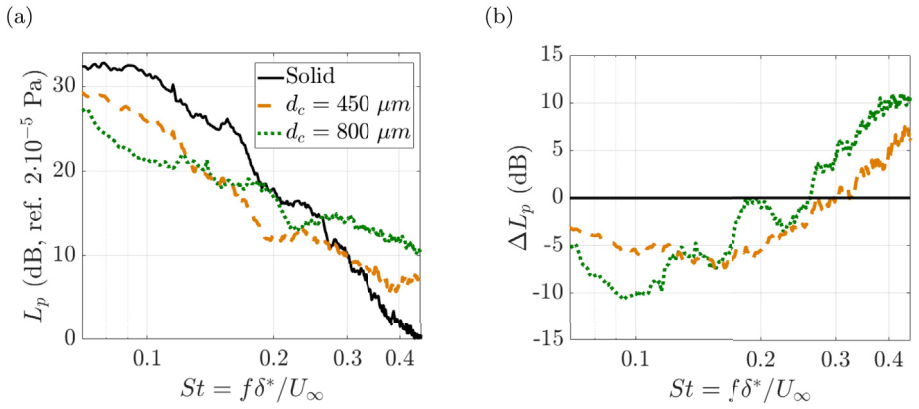

Fig. 11. Sound Pressure Level L_p measured with the microphone phased array for the solid and permeable trailing edge inserts. The acoustic energy corresponds to a 6.1 Hz band. These values correspond to an observer placed at the center of the array. (a) Absolute values. (b) Relative values with respect to the solid case.

3. Results and discussion

3.1. Far-field noise measurements

Trailing edge noise for both permeable inserts and the solid case are presented in Fig. 11(a). The results are expressed in terms of Sound Pressure Level L_p in decibels relative to $p_{\text{ref}} = 20$ μPa, defined by:

$$L_p = 10\log_{10}\left(\frac{\overline{p^2}}{p_{\text{ref}^2}}\right) \tag{11}$$

as a function of the Strouhal number St based on the displacement thickness δ^* and the free-stream velocity U_∞. Note that the δ^* values used in St are measured at $x/c = -0.02$ for each trailing edge insert, and are reported later in section 3.2.1.

It is interesting to note that the spectra show different slopes depending on the type of porous insert. This might be indicative of a modification of the noise source (turbulent flow) and/or the radiation efficiency of the edge, i.e. reduction in the acoustic impedance discontinuity. More in detail, up to $St = 0.26$ spectra measured for the $d_c = 450$ μm metal foam insert shows similar slope to the baseline case, while the $d_c = 800$ μm insert shows a larger slope. For the $d_c = 450$ μm case, the spectra is shifted towards lower L_p values suggesting that the impedance discontinuity might not be strongly affected by the porous insert, but the energy of the source, i.e. turbulent fluctuations, decreases. Such hypothesis is investigated in detail in the remainder of the manuscript.

Spectra for both porous treatments have similar slopes above $St = 0.28$, denoting that noise within this St range is related to the same phenomena. The fact that porous treatments cause equal or higher noise production than the solid insert, and that L_p is increased with cell size suggests that this high-St noise contribution can be attributed to surface roughness noise [46]. This was demonstrated [74] by stopping the flow communication between suction and pressure sides for a trailing edge manufactured with open-cell metal foam.

The difference between far-field noise for the porous treatments with respect to the solid insert $\Delta L_p = L_p^{\text{porous}} - L_p^{\text{solid}}$ is shown in Fig. 11(b). It shows noise abatement below cross-over $St = 0.26$ (1.6 kHz) and $St = 0.3$ (1.9 kHz) for metal foams with $d_c = 800$ μm and $d_c = 450$ μm, respectively. Noise abatement below $St = 0.12$ is larger for the $d_c = 800$ μm metal foam insert; a maximum noise decrease of 11 dB is measured at $St = 0.09$. On the other hand, the $d_c = 450$ μm metal foam treatment leads to the lowest measured ΔL_p values within the range $St = 0.16$–0.3; it is precisely at the beginning of this range where a maximum noise attenuation of 7 dB is measured. The results confirm that the use of higher permeability metal foam treatments leads to larger noise abatement, in agreement with Herr et al. [26]; however, the frequency range where noise reduction is measured is smaller. This observation also holds for data reported in the aforementioned study, where noise reduction up to 11 kHz was achieved with different low permeability/high resistivity metal foams (up to $R = 278$ kNs/m^4 at $\text{Re} = 1 \times 10^6$). Finally, noise increase with respect to the solid trailing edge is measured above the cross-over St. Maximum excess noise ΔL_p values of 8 and 10 dB are respectively observed for $d_c = 450$ μm and $d_c = 800$ μm metal foam inserts at a $St = 0.45$.

In order to assess the general noise reduction performance of the metal foam inserts as perceived by the human ear, the overall A-weighted Sound Pressure Level L_A [75] is presented in Table 3. It is found that metal foam inserts cause a considerable reduction of the L_A with respect to the baseline case: 4.8 dBA and 6.4 dBA for the $d_c = 450$ μm and the $d_c = 800$ μm metal foam inserts respectively; hence, in spite of the high-frequency noise increase described above, the use of open-cell metal foams at the trailing edge represents an effective strategy for noise abatement.

Table 3
Measured L_A for the solid and metal foam inserts.

	L_A (dBA)
Solid	48.4
$d_c = 450$ μm	43.6
$d_c = 800$ μm	42

Table 4
Comparison of boundary layer parameters at the trailing edge reported in previous studies and XFOIL with data measured at $x/c = -0.02$ above the solid insert.

Investigation	δ^* (mm)	θ (mm)	δ_{99} (mm)	H	$C_f(\times 10^{-3})$
Present	3.2	1.6	9.3	2	1.6
Arce León et al. [35]	2.1	1.3	9.4	1.6	1.9
Avallone et al. [32]	3.3	1.5	9.5	2.2	–
XFOIL [36]	2.3	1.2	–	2	1.1

3.2. Flow field

In this section, a description of the flow-field for the three measured cases is presented. In order to investigate whether changes within the boundary layer due to porous inserts support the observed changes in noise production, the properties of the mean and turbulent flow field, and the quantities described in section 2.3 are further investigated and compared. The analysis is performed in the $x - y$ coordinate system, at three different locations to characterize the evolution of the boundary-layer flow-field: $x/c = -0.08$, $x/c = -0.05$ and $x/c = -0.02$.

3.2.1. Mean flow field

The analysis of the boundary layer mean flow above the permeable and solid trailing edge is performed on the dataset containing uncorrelated PIV snapshots. First, data measured above the solid trailing edge insert are compared to previous studies.

The boundary layer displacement thickness δ^* and momentum thickness θ are calculated following the method proposed by Spalart and Watmuff [76]. In this formulation, the integrals are truncated at the edge of the boundary layer δ_e, taken as the position where the integral of the vorticity along the wall-normal direction $\int \omega_z dy$ stabilizes.

Values of δ^* and θ near the trailing edge ($x/c = -0.02$) are compared with those obtained in previous experimental studies [32,35] and XFOIL [36] for a similar test case (solid NACA 0018, $\alpha = 0°$, $\mathrm{Re} = 2.6 \times 10^5$) in Table 4. For completeness, values of the boundary layer thickness δ_{99}, defined such as $U(\delta_{99}) = 0.99U_e$, and the shape factor $H = \delta^*/\theta$ are also presented. Quantities obtained in the present investigation show good agreement with the experimental data presented in Avallone et al. [32], while they overestimate the values of Arce León et al. [35] and XFOIL [36]. This discrepancy is likely caused by the use of a different tripping element.

The friction coefficient $C_f = \tau_w/(0.5\rho U_\infty^2)$, where τ_w refers to wall shear stress, is also presented in Table 4. This quantity cannot be evaluated directly since data are not available close to the wall; for this reason, the Clauser chart method [77] is employed to calculate it. The method retrieves C_f through a fit of measured data to the logarithmic law, defined by:

$$U^+ = \frac{1}{\kappa} \ln\left(y^+\right) + C \tag{12}$$

where $\kappa = 0.4$ and $C = 5$. The logarithmic law is expressed in terms of wall units $U^+ = U/U_\tau$ and $y^+ = yU_\tau/\nu$, where $U_\tau = \sqrt{\tau_w/\rho}$ represents the friction velocity and ν the kinematic viscosity. As seen in Table 4, C_f values obtained through this method show good agreement with experimental data presented in Arce León et al. [35] and XFOIL.

Profiles of the mean wall-parallel velocity component U for the three configurations are compared in Fig. 12(a)–(c). The y-axis and U are respectively normalized with the boundary layer thickness δ_{99} and the free-stream velocity U_∞. Data are shown between $0.2 < y/\delta_{99} < 1.4$. The results at $x/c = -0.08$ show a less full velocity profile for both permeable cases, becoming emptier for increasing permeability values (increasing cell diameter). Decrease in U/U_∞ with respect to the solid surface, i.e. a velocity deficit, occurs within $0.5 < y/\delta_{99} < 0.8$ for the $d_c = 450$ μm foam insert, while it affects the whole profile for the $d_c = 800$ μm foam. The velocity deficit is also found in previous experiments on rough surfaces [78,79] or porous trailing edge inserts [25] and it is attributed to higher surface drag caused by roughness.

It is also seen that independently on the material U decreases in the streamwise direction outside the boundary layer; this is attributed to the divergence of the streamlines from the wall-parallel direction. Conversely, the material influences the magnitude of the adverse pressure gradient within the boundary layer; at outer boundary layer positions ($y/\delta_{99} > 0.4$), the solid surface allows higher velocity at $x/c = -0.08$, while at $x/c = -0.02$ higher or similar velocity values are measured above permeable inserts. This indicates that the porous treatments decrease the magnitude of the adverse pressure gradient within this region. On the other hand, within the inner region the velocity deficit becomes larger for increasing x/c. Hence, a stronger

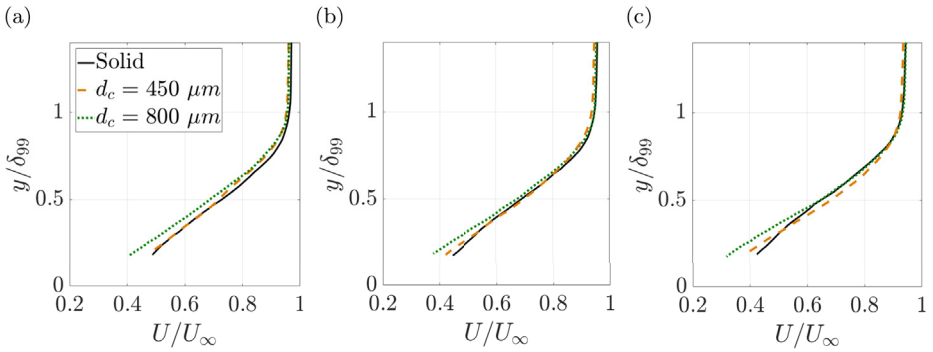

Fig. 12. Mean wall-parallel velocity U/U_∞ variation along the wall-normal direction y/δ_{99} for the three configurations. Three different streamwise locations are shown: $x/c = -0.08$ (a), $x/c = -0.05$ (b) and $x/c = -0.02$ (c).

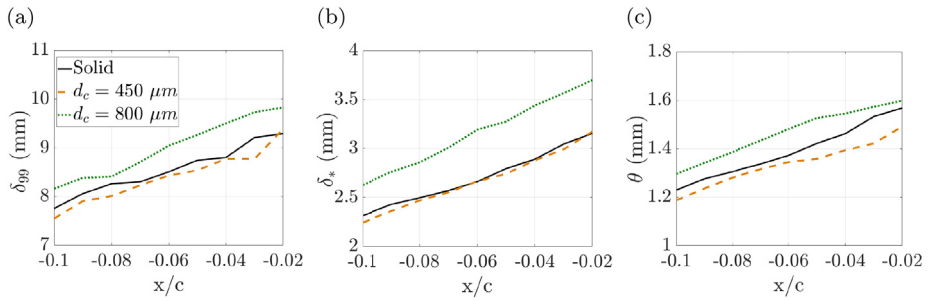

Fig. 13. Boundary layer thickness δ_{99} (a), displacement thickness δ^* (b) and momentum thickness θ (c) variation with dimensionless streamwise coordinate x/c above the solid and permeable trailing edge inserts.

adverse pressure gradient takes place due to the use of permeable materials.

In Fig. 13, the boundary layer thickness δ_{99} (a), displacement thickness δ^* (b) and momentum thickness θ (c) for the three trailing edge inserts are compared. Note that boundary layers over solid and permeable walls have different characteristics, i.e. the classic no-slip condition present at solid surfaces does not apply on permeable walls. In the present study, the method previously described to calculate δ_{99}, δ^* and θ over the solid surface is also applied on permeable walls, neglecting flow through the foam insert.

It is found that all the integral quantities have larger values for the $d_c = 800$ μm metal foam insert. On the other hand, δ_{99} and δ^* measured above the $d_c = 450$ μm metal foam are similar to the solid insert, whereas θ is lower. These results point out the dependence of the boundary layer topology on the characteristics of the metal foam. Increase of δ_{99}, δ^* and θ with permeability is reported in Geyer et al. [24] on fully porous airfoils. The fact that here the increase is measured only over one type of the metal foam might be explained by the shorter porous extension employed.

Increase of δ^* and θ for the $d_c = 800$ μm metal foam insert with respect to the solid case is caused by the velocity deficit described previously, which leads to an increased mass and momentum deficit. The velocity deficit is also present above the $d_c = 450$ μm metal foam insert, although its magnitude is smaller. In this case, the mass and momentum deficits are balanced by the increase of U at the outer boundary layer region, also described above. It can be concluded that only the $d_c = 800$ μm porous treatment causes significant changes in the boundary layer topology with respect to the baseline case, whereas the $d_c = 450$ μm and the solid insert lead to similar results. This result is in line with the noise reduction features described in section 3.1.

Mean wall-normal velocity V/U_∞ profiles are plotted in Fig. 14(a)–(c). Results show that increasing the cell diameter (i.e. the permeability) of the metal foam leads to larger V; considering that U decreases with K, it is concluded that the permeability enhances the divergence of the streamlines from the wall. The V profiles for the three configurations vary in the streamwise direction showing smaller differences at the trailing edge; these phenomena might be linked to a weak flow recirculation within the porous medium, as observed by Showkat Ali et al. [80].

3.2.2. Turbulent flow field

In Fig. 15(a)–(c), profiles of the r.m.s. wall-parallel velocity $\sqrt{\overline{u^2}}/U_\infty$ are plotted. The results show reduction of $\sqrt{\overline{u^2}}/U_\infty$ within a major part of the boundary layer due to the porous treatment. In the present investigation, a larger reduction in turbulence levels is measured for the metal foam with smaller d_c, i.e. lower permeability.

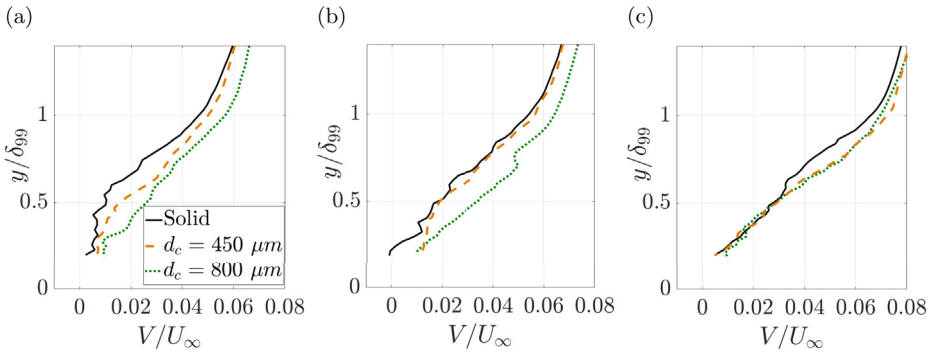

Fig. 14. Mean wall-normal velocity V/U_∞ at three streamwise locations: $x/c = -0.08$ (a), $x/c = -0.05$ (b) and $x/c = -0.02$ (c).

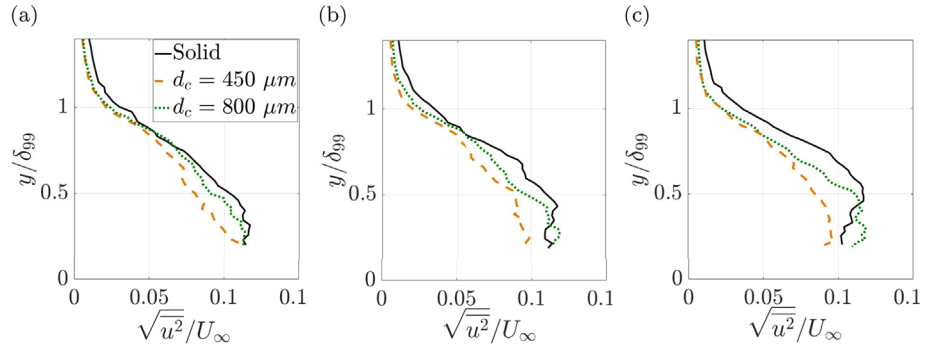

Fig. 15. R.m.s. wall-parallel velocity $\sqrt{\overline{u^2}}/U_\infty$ at three different streamwise locations: $x/c = -0.08$ (a), $x/c = -0.05$ (b) and $x/c = -0.02$ (c).

More specifically, decrease in $\sqrt{\overline{u^2}}/U_\infty$ with respect to the reference case is found above the $d_c = 450$ μm metal foam insert independently of x or y. Conversely, a dependence on the location is found for the $d_c = 800$ μm porous insert; while at $x/c = -0.08$ turbulence intensity is always lower or equal to the solid case, an increase is measured closer to the wall at $x/c = -0.05$ and $x/c = -0.02$.

The analysis of the r.m.s. wall-normal velocity profiles $\sqrt{\overline{v^2}}/U_\infty$, plotted in Fig. 16(a)–(c), yields similar conclusions: as for $\sqrt{\overline{u^2}}/U_\infty$, permeable inserts allow a general reduction of $\sqrt{\overline{v^2}}/U_\infty$ with respect to the solid surface. Again, the reduction is larger for the metal foam insert with lower permeability ($d_c = 450$ μm). Conversely, no increase in $\sqrt{\overline{v^2}}/U_\infty$ with respect to the reference case is measured independently of the location or type of foam.

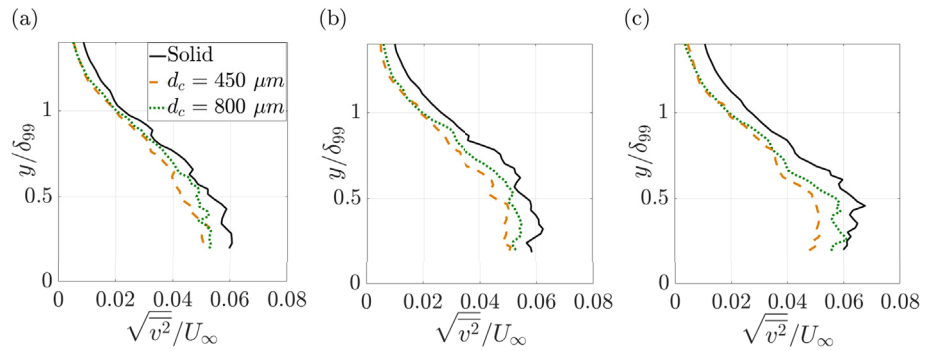

Fig. 16. R.m.s. wall-normal velocity $\sqrt{\overline{v^2}}/U_\infty$ at three different streamwise locations: $x/c = -0.08$ (a), $x/c = -0.05$ (b) and $x/c = -0.02$ (c).

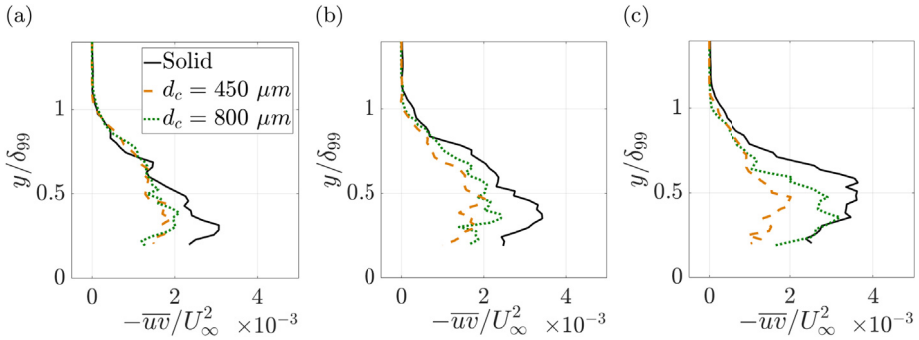

Fig. 17. Reynolds stress $-\overline{uv}/U_\infty^2$ at three different streamwise locations are shown: $x/c = -0.08$ (a), $x/c = -0.05$ (b) and $x/c = -0.02$ (c).

Reduction of turbulence intensity within the outer boundary layer region due to permeable metal foams was also found in Showkat Ali et al. [18] on experiments on a flat plate with a permeable extension. Similarly to the present results, increase in $\sqrt{\overline{u^2}}/U_\infty$ with respect to the solid case, attributed to the increase of friction along the rough surface, was limited to the inner part of the boundary layer. Nevertheless, in previous experimental research on porous trailing edge inserts on asymmetric airfoils at incidence [81], an increase of the r.m.s. velocity fluctuations at the suction side above porous treatments was reported. This discrepancy might be due to the different set-up; the imbalance of pressure between suction and pressure side of the trailing edge caused by the incidence leads to a steady cross-flow blowing within the measurement location, which is known to increase the turbulence intensity in boundary layers [82].

Interestingly, permeable inserts bring the maximum level of turbulence closer to the wall; for solid edges, this is supposed to increase the scattering efficiency, hence far-field noise [83], in disagreement with results described in section 3.1. The difference might be explained by the permeability of the inserts, which might reduce the acoustic impedance jump at the edge through the presence of unsteady flow inside the insert; this hypothesis is supported by the change of slope of acoustic spectra reported above for the most permeable foam insert.

The apparent lack of correlation between the flow field statistics and the far-field acoustic emission of permeable inserts might also be contributed by the fact that the surface slope of a rough surface acts as a filter between the wall-pressure wavenumber spectrum and the far-field acoustic emission [84].

For boundary layer analysis, the Reynolds shear stress $-\overline{uv}/U_\infty^2$ is used to describe coherent turbulent motions [85]. In Fig. 17(a)–(c), profiles of $-\overline{uv}/U_\infty^2$ at $x/c = -0.08$, $x/c = -0.05$ and $x/c = -0.02$ are shown. It is found that metal foam inserts lead to decreased $-\overline{uv}/U_\infty^2$ values within the boundary layer, indicating that permeable treatments reduce the energetic content of coherent structures responsible for momentum transfer to and away from the wall and usually related to wall-pressure fluctuations [86]. In agreement with $\sqrt{\overline{u^2}}/U_\infty$ and $\sqrt{\overline{v^2}}/U_\infty$, the lowest Reynold shear stress values are measured above the less permeable metal foam insert ($d_c = 450$ μm). The fact that the decrease of the energy of the fluctuations does not vary linearly with permeability could be related to the presence of flow through the insert, as hypothesized previously, that can promote stronger vortices for metal foam inserts with higher permeability. It is also interesting to note that for the baseline case the $-\overline{uv}/U_\infty^2$ hump becomes broader and moves away at more downstream locations; this effect is less strong for the porous inserts.

The previous analysis has shown that permeable treatments affect the characteristics of turbulent flow; to further investigate this aspect, a quadrant analysis is performed. With this technique, the instantaneous fluid motions contributing to the total Reynolds shear stress $-\overline{uv}$ are assigned to the quadrant Q_n ($n \in [1,2,3,4]$) in terms of the sign of u and v [87]. The classification is performed as follows

$$Q_1 \in \{u > 0, v > 0\} \tag{13a}$$

$$Q_2 \in \{u < 0, v > 0\} \tag{13b}$$

$$Q_3 \in \{u < 0, v < 0\} \tag{13c}$$

$$Q_4 \in \{u > 0, v < 0\} \tag{13d}$$

In wall-bounded flows, the larger contribution to the total Reynolds stress is due to events in Q_2 and Q_4, which respectively account for ejections of low-momentum fluid away from the wall and sweeps of high-momentum fluid towards the wall [88].

An example of quadrant analysis is shown in Fig. 18 together with the hyperbolae $|uv| = -5\,\overline{uv}$, which are used to identify the intense events, i.e. turbulent motions in which the instantaneous Reynolds shear stress is at least 5 times larger than the mean Reynolds stress $\overline{uv}$ (events outside the hyperbolae). These events can be related to high amplitude wall-pressure peaks

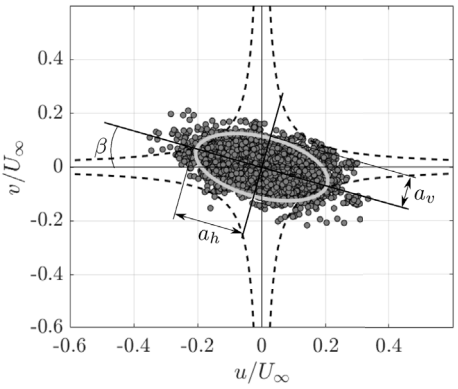

Fig. 18. Example of quadrant analysis performed at $(x/c = -0.04, y/\delta_{99} = 0.3)$ in the baseline case. The hyperbolae $|\ uv\ | = -5\ \overline{uv}$ are plotted with a black dashed line. The fitted ellipse is depicted in grey. The set of parameters defining the ellipse (β, a_h, a_v) is also sketched.

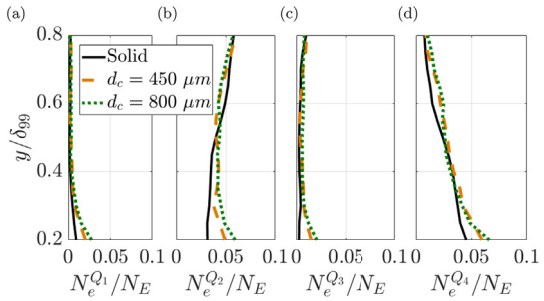

Fig. 19. Variation of the fraction of intense events $N_e^{Q_n}/N_E$ in each quadrant with y. (a) Q_1 (b) Q_2 (c) Q_3 (d) Q_4.

[89,90], being then relevant for trailing edge noise. The choice of a constant value equal to 5 is based on previous studies [91,92] on wall-bounded flows. In order to improve the quality of the statistical analysis, the vector spacing is increased to 0.72 mm; thus, each quadrant analysis contains a total of $N_E = 3276$ events.

The number and the energy budget of intense events in Q_n are respectively quantified by the fraction of intense events $N_e^{Q_n}/N_E$ and their contribution to the total Reynolds shear stress $\overline{uv}_e^{Q_n}$, calculated as

$$\overline{uv}_e^{Q_n} = \frac{\sum_{m=0}^{m=N_e^{Q_n}} uv_{e,m}^{Q_n}}{N_E} \tag{14}$$

Since it has been verified that $N_e^{Q_n}/N_E$ and $\overline{uv}_e^{Q_n}$ do not depend on the x location, data within $-0.08 < x < -0.02$ are further averaged in the streamwise direction. Furthermore, data measured within $0.8 < y/\delta_{99} < 1$ are not shown since within this region $-\overline{uv}$ is low.

The variation of $N_e^{Q_n}/N_E$ with y is plotted in Fig. 19(a)–(d) for the four quadrants. Results show that, above the solid trailing edge insert, the majority of intense events are in Q_2 and Q_4, with ejection and sweep motions being predominant within the outer and inner boundary layer, respectively. Similar findings are reported in previous research [35,90], where they were linked to the appearance of hairpin-like vortices within the boundary layer.

It is found that metal foam inserts alter significantly the intense events distribution along y independently on the quadrant. Within the outer region $(y/\delta_{99} > 0.5)$, porous treatments decrease $N_e^{Q_2}/N_E$ up to 0.01, while $N_e^{Q_4}/N_E$ increases by the same magnitude. More interestingly, closer to the wall the number of intense events in all the quadrants increases due to the porous treatments; a maximum increase of 0.02 N_E in Q_1, Q_3 and Q_4, and about 0.03 N_E in Q_2 is always measured at $y/\delta_{99} = 0.2$ above the most permeable insert.

The increase of the number of intense events close to the wall with increasing permeability of the treatment might be linked to the cross-flow through the foam. This hypothesis is further supported by the increase of intense events within Q_1 and Q_3, which are residual in conventional boundary layer flows; hence, the flow inside the foam insert would cause streamwise ejection and upstreamwise sweeping motions. This scenario is also in agreement with the fact that, contrarily to the solid insert, the maximum $-\overline{uv}/U_\infty^2$ value for the porous treatments remains close to the wall independently of the streamwise position, as described above.

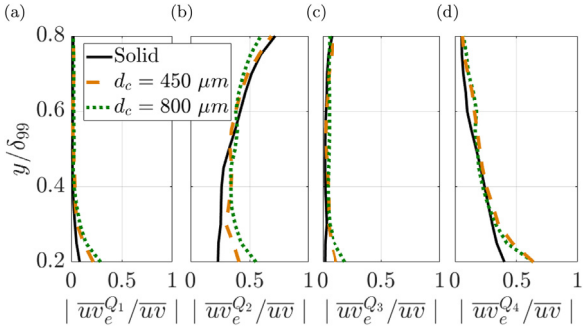

Fig. 20. Change with y of the absolute contribution of the intense events in each quadrant to the total Reynolds shear stress $|\ \overline{uv}_e^{Q_n}/\overline{uv}\ |$. (a) Q_1 (b) Q_2 (c) Q_3 (d) Q_4.

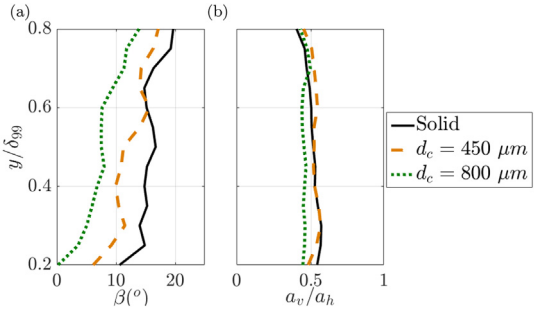

Fig. 21. Change with y of the streamwise averaged tilt angle β (a) and ratio of vertical-to-horizontal axis length a_v/a_h (b).

The analysis of the absolute contribution of intense events in each quadrant to the total Reynolds shear stress $|\ \overline{uv}_e^{Q_n}/\overline{uv}\ |$, shown in Fig. 20(a)–(d), supports the previous hypothesis: since the number of intense events is increased near the wall, the relative contribution of the intense events to the total Reynolds stress is also increased.

Besides the number and the intensity, the distribution of intense events within the quadrants can also provide relevant information about the vortex structure within the boundary layer, as suggested by Suga et al. [93]. In order to quantitatively discuss this aspect, at each boundary layer location an ellipse centred at $(u = 0, v = 0)$ is least-squares fitted to the entire ensemble of events.

As in Suga et al. [93], three parameters (depicted in Fig. 18) are used to characterize the ellipse: the tilt angle with respect to the u-axis β, and the semi-major a_h and semi-minor a_v axes. Similarly to the analysis of $N_e^{Q_n}/N_E$ and $\overline{uv}_e^{Q_n}/\overline{uv}$, it is found that the variation of β, a_h and a_v with x is negligible. Therefore, data are streamwise averaged and the variation of the fitting parameters with y is obtained. The tilt angle β and the ratio of vertical-to-horizontal axis a_v/a_h are respectively plotted in Fig. 21(a) and (b).

Results show that the ratio a_v/a_h is constant and approximately equal to 0.5 independently of the insert or wall-normal position. Note that this does not imply that the size of the ellipse is equal for all the inserts, but that the aspect ratio of the ellipses is similar. More interestingly, a significant decrease of β due to porous treatments is found: lower values of β are reported for increasing permeability of the metal foam and decreasing y. The fact that the change in β due to porous treatments takes place along the entire boundary layer indicates that it is mainly caused by the reduction of the v component of the intense events in Q_2 and Q_4, while the u component is similar or higher. In other words, porous treatments enhance the anisotropy of highly energetic turbulent motions by stretching the flow in the x direction. This has consequences on trailing edge noise production of porous inserts; as seen in Eq. (5), the wall-normal velocity is related to the generation of surface pressure fluctuations, which are the source for broadband trailing edge noise. Therefore, the stretching of these intense ejection (Q_2) and sweeping motions (Q_4) due to porous treatments might be responsible for the previously observed low-frequency noise reduction.

3.2.3. Velocity power spectra

Considering the relevant differences in the turbulent field reported in section 3.2.2 and their implications on noise production, it is worthwhile to analyse the spectra to determine which spectral range is affected by the porous treatments.

The power spectral density of the wall-parallel velocity fluctuations Φ_{uu} at $x/c = -0.02$ is shown in Fig. 22 for the three cases. Data at $x/c = -0.08$ and $x/c = -0.05$ are not plotted for the sake of conciseness. Two different wall-normal locations, $y/\delta_{99} = 0.4$ and $y/\delta_{99} = 0.8$, are presented to analyse the effect of the permeable inserts on Φ_{uu} across different regions of the boundary layer.

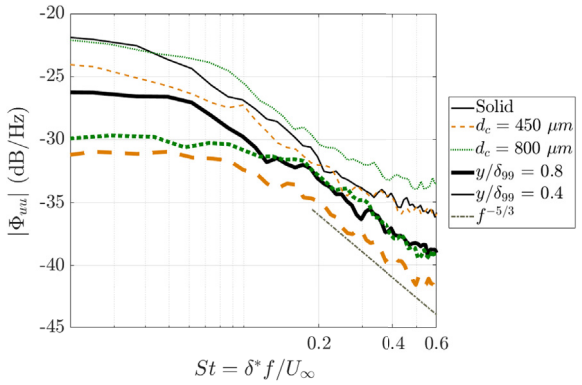

Fig. 22. Spectral density of the wall-parallel velocity fluctuations Φ_{uu} at $x/c = -0.02$. In each plot, data measured at $y/\delta_{99} = 0.4$ and $y/\delta_{99} = 0.8$ are presented. Dashed-dotted line refers to Kolgomorov −5/3 decay law.

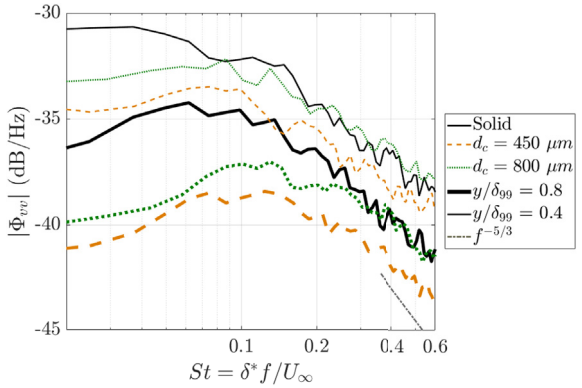

Fig. 23. Spectral density of the wall-normal velocity fluctuations Φ_{vv} at $x/c = -0.02$. Legend as in Fig. 22.

It has to be taken into account that the temporal resolution is limited by PIV, with the frequency analysis of the measured signals being restricted to 3/4 of the Nyquist frequency [89]. Hence, the following analysis is limited to $f = 3.75$ kHz, i.e. $St \simeq 0.5$. Fig. 22 reveals that only the spectra measured at $y/\delta_{99} = 0.8$ follows the −5/3 Kolmogorov decay [94] correctly up to $St = 0.5$, where it becomes flattened. Data measured closer to the wall ($y/\delta_{99} = 0.4$) presents a plateau in the spectra starting at a frequency of approximately 3 kHz ($St \simeq 0.4$). Such phenomena takes place because of lower signal-to-noise ratio due to the presence of laser reflections near the wall.

Results show higher turbulence energy at $y/\delta_{99} = 0.4$ independently on the insert, in agreement with results discussed in section 3.2.2. At $y/\delta_{99} = 0.8$, the $d_c = 450$ µm porous treatment causes a decrease in Φ_{uu} with respect to the baseline case across the entire St range, with a maximum difference of 5 dB at the lowest reported $St = 0.02$. Conversely, for the $d_c = 800$ µm metal foam insert a decrease of Φ_{uu} with respect to the solid case is only measured up to $St = 0.12$, with a maximum reduction of 4 dB at $St = 0.06$; above the cross-over St the spectral content is similar to the solid case. Closer to the wall, it is observed that the $d_c = 450$ µm insert only leads to attenuation of Φ_{uu} below $St = 0.2$, with maximum reduction of 3 dB at $St = 0.04$. At this wall-normal position, Φ_{uu} levels measured above the $d_c = 800$ µm foam insert are similar (below $St = 0.04$) or slightly higher than the baseline case (up to 2 dB).

The spectra of the wall-normal velocity fluctuations, Φ_{vv}, at $x/c = -0.02$ is presented in Fig. 23. The magnitude of Φ_{vv} is considerably lower than the wall-parallel component; hence, the signal-to-noise ratio is lower with respect to the one of Φ_{uu}. The analysis of Φ_{vv} yields similar conclusions to those of the wall-parallel component. At $y/\delta_{99} = 0.8$, the $d_c = 450$ µm permeable treatment leads to attenuation of Φ_{vv} with respect to the baseline case independently of the St, with a maximum difference of 5 dB at the lowest measured St. The $d_c = 800$ µm insert causes a decrease in Φ_{vv} below $St = 0.33$, with a maximum decrease of 4 dB at the same St. At $y/\delta_{99} = 0.4$, the magnitude of the maximum reduction with respect to the solid surface is decreased to 4 dB for the $d_c = 450$ µm metal foam insert. The $d_c = 800$ µm metal foam insert leads to attenuation in Φ_{vv} below $St = 0.09$; above this St, the porous insert and the baseline case show similar Φ_{vv} values.

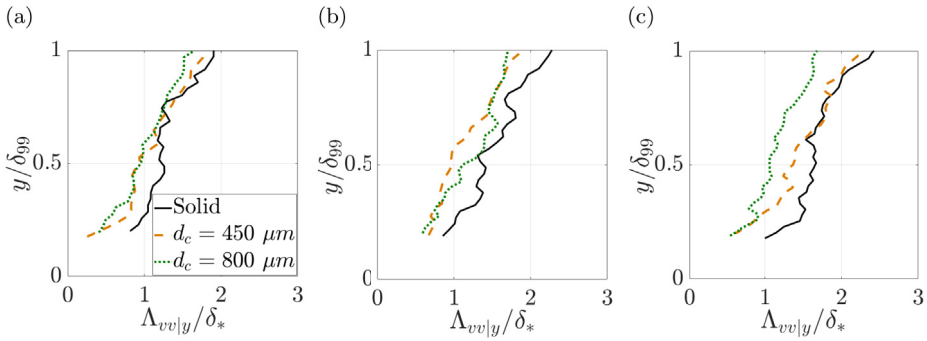

Fig. 24. Variation of $\Lambda_{vv|y}(x,y)/\delta_*$ across the boundary layer at three different streamwise locations: $x/c = -0.08$ (a), $x/c = -0.05$ (b) and $x/c = -0.02$ (c).

Assuming Taylor's "frozen turbulence" hypothesis[2] noise radiation at a certain frequency f is only due to turbulence being convected over the trailing edge with streamwise wavenumber $k = 2\pi f/U_c$ [30,53]. Therefore, the reduction of Φ_{uu} and Φ_{vv} within the low frequency range can be linked to noise attenuation. For the $d_c = 450$ μm porous insert, low frequency noise attenuation and velocity fluctuation spectra variation with respect to the baseline case have approximately the same magnitude, which suggest that the reduction of the energy of the source might be a significant contributor for the change in the low frequency acoustic scattering with respect to the solid edge. This is supported by the fact that both inserts share similar boundary layer topology and slope of the acoustic spectra. Conversely, larger low frequency noise attenuation is found for the metal foam insert with higher permeability ($d_c = 800$ μm), in disagreement with the measured velocity fluctuation spectra. A hypothesis that would explain this inconclusive result is that the reduction of turbulence energy within the boundary layer is only partially accountable for noise reduction, while other mechanisms arise. One of these might be the change of the structure of highly energetic turbulent motions reported in section 3.2.2. Another aspect of noise scattering by permeable inserts that remains unclear is the previously reported high frequency noise increase with respect to the baseline case; the changes of the velocity spectra within that frequency range do not support such a feature.

3.2.4. Wall-normal integral length scale

As seen in Eq. (5), $\Lambda_{vv|y}/\delta_*$ can be used to link the size of turbulence structures with wall-pressure fluctuations in solid edges. For this reason, the wall-normal distribution of $\Lambda_{vv|y}/\delta_*$ at three different streamwise locations, $x/c = -0.08$, $x/c = -0.05$ and $x/c = -0.02$, are respectively presented in Fig. 24(a)–(c) for wall-normal positions $0.2 < y/\delta_{99} < 1$.

It is observed that, at $x/c = -0.02$, $\Lambda_{vv|y}/\delta_*$ is between 1 and 2.5 times the displacement thickness at that location; comparable values are found in Arce León et al. [35] and Kamruzzaman et al. [96] at the trailing edge of a NACA 0018 airfoil measured in similar aerodynamic conditions.

At $x/c = -0.08$ (Fig. 24 (a)), it can be seen that permeable inserts modify significantly $\Lambda_{vv|y}$ only below $y/\delta_{99} = 0.6$, where a maximum relative decrease with respect to the solid edge of 50% is reported. At more downstream positions a decrease of $\Lambda_{vv|y}$ with respect to the baseline case is also observed, with its magnitude depending on the metal foam and the location. For instance, at $x/c = -0.05$ (Fig. 24 (b)), a reduction of $\Lambda_{vv|y}$ is measured for the $d_c = 450$ μm porous treatment along the entire boundary layer. Conversely, closer to the trailing edge (Fig. 24 (c)), the $d_c = 800$ μm metal foam insert shows reduction for the entire boundary layer. At this streamwise position, a maximum relative reduction of 50% with respect to the solid case is measured above both porous materials.

$\Lambda_{vv|y}$ is related to the largest wall-normal turbulence scale present within the boundary layer [97]; therefore, the decrease of this quantity with increasing permeability of the porous treatment at $x/c = -0.02$ is in agreement with the stretching of strong turbulent motions reported in section 3.2.2. This indicates that porous treatments not only reduce the turbulent kinetic energy associated to the wall-normal velocity component of these motions but also their extent. The fact that, close to the edge, the wall-normal length scale decreases with the permeability of the insert suggests that it is also relevant for noise reduction for permeable treatments.

3.2.5. Wall-parallel convection velocity

Finally, the last turbulence quantity included in Eq. (5) that is addressed in the present manuscript is the convection velocity U_c.

Fig. 25 plots the convection velocity U_c/U_∞ profiles measured at $x/c = -0.02$; only this streamwise location is shown since it is found that its magnitude does not vary significantly with x. The streamwise convection velocity measured over the solid surface ranges between 0.5 and $0.9U_\infty$. Similar values are found in Arce León et al. [35]. The permeable treatments produce a

[2] To the authors' knowledge, there is no available study about the convenience of assuming Taylor's hypothesis over permeable walls. However, frozen turbulence is known to be a reasonable assumption over rough walls for the flow dominant velocity component [95].

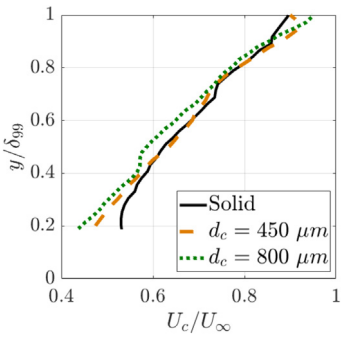

Fig. 25. Wall-parallel convection velocity U_c/U_∞ at $x/c = -0.02$.

general decrease in the streamwise convection velocity, with stronger attenuation for increasing values of permeability/pore size. Relative reductions compared to the solid case of up to 11% and 20% are measured respectively for the $d_c = 450$ μm and $d_c = 800$ μm inserts. Small regions where convection velocity increases up to a 5% due to porous materials are also measured, although they are usually confined to outer positions ($y/\delta_{99} > 0.9$).

Reduction of U_c measured over permeable inserts might also contribute to noise abatement within the low frequency range. To support this, maximum decrease in U_c/U_∞ and L_p with respect to the baseline airfoil is found over the same metal foam insert ($d_c = 800$ μm). However, the small difference between U_c measured above both permeable inserts seems unlikely to be able to explain alone the very different magnitude of low frequency noise abatement.

4. Conclusions

An experimental aeroacoustic study of a NACA 0018 airfoil with solid and porous trailing edge inserts covering 20% of the chord length is performed. Far-field noise is measured by means of a phased microphone array. Low frequency noise attenuation of up to 7 and 11 dB are respectively observed for the $d_c = 450$ μm and $d_c = 800$ μm metal foam inserts at $St = 0.16$ and $St = 0.09$. Conversely, at higher frequencies up to 8 and 10 dB noise increase, caused by surface roughness, are reported. A reduction of the frequency range affected by noise attenuation with increasing permeability is also described.

Planar PIV measurements are employed to monitor the flow field over the inserts. The analysis of the boundary layer reveals important variations in the mean flow and turbulence properties. In particular, increase of the boundary layer and displacement thickness with respect to the solid case is measured for the metal foam insert with higher permeability. However, the $d_c = 450$ μm metal foam and solid inserts have similar boundary layer topology. A decrease of the mean wall-parallel velocity, attributed to a higher surface drag, is reported for the insert with larger cell size. Relevant changes in the turbulence intensity and Reynolds shear stress due to metal foam treatments are also described; a decrease of these quantities is reported, with lower values being measured for the $d_c = 450$ μm insert. Further analysis in the frequency domain show that the attenuation of velocity fluctuations affects mostly the low frequency range: a maximum reduction of 5 and 4 dB are respectively measured at $St = 0.02$ for $d_c = 450$ μm and $d_c = 800$ μm metal foam inserts. In view of these results, it is proposed that the reduction of turbulence velocity fluctuations might be one of the changes contributing to noise abatement, particularly for the $d_c = 450$ μm insert. Conversely, a relevant increase of high frequency fluctuations content with respect to the solid case, which would support reported high frequency noise increase, is not observed. Further insight into the properties of highly energetic turbulent motions within the boundary layer is obtained through the quadrant analysis. This technique suggests a milder acoustic impedance jump at the edge, which would benefit noise abatement. It also reveals that the permeability decreases the amplitude of the wall-normal velocity component of such motions, i.e., it enhances their anisotropy; this modification can be linked to low frequency trailing edge abatement. To support this finding, the analysis of the wall-normal integral scale shows up to 50% reduction with respect to the baseline case, with larger reduction being measured for the insert with higher permeability. Finally, it is found that porous treatments decrease the streamwise convection velocity, with a maximum reduction relative to the solid surface of 20% measured for the $d_c = 800$ μm insert. It is therefore concluded that the variation of this quantity also supports low frequency noise attenuation.

The previously described modifications of boundary layer properties do not fully explain reported changes in acoustic scattering of porous edges. Thus, the contribution of other likely causes for trailing edge noise production in porous treatments, such as the modification of the acoustic impedance of the edge or the reduction in spanwise coherence of the wall-pressure fluctuations, requires further assessment.

Acknowledgements

The authors are grateful for the contribution of G.R.A.S. and NI to the preparation of the beamforming setup and the support in the foam research. In particular the authors would like to acknowledge Niklas B. Larsen, Per Rasmussen and Alex Floor for

their outstanding participation and support. This research did not receive any specific grant from funding agencies in the public, commercial, or not-for-profit sectors.

References

[1] T.F. Brooks, D.S. Pope, M.A. Marcolini, Airfoil Self-noise and Prediction, Tech. Rep. 19890016302, National Aeronautics and Space Administration, 1989.
[2] S. Oerlemans, P. Sijtsma, B.M. Lopez, Location and quantification of noise sources on a wind turbine, J. Sound Vib. 299 (4–5) (2007) 869–883, https://doi.org/10.1016/j.jsv.2006.07.032.
[3] A. Wolf, T. Lutz, W. Würz, E. Krämer, O. Stalnov, A. Seifert, Trailing edge noise reduction of wind turbine blades by active flow control, Wind Energy 18 (5) (2014) 909–923, https://doi.org/10.1002/we.1737.
[4] M. Szoke, M. Azarpeyvand, Active flow control methods for the reduction of trailing edge noise, in: 23rd AIAA/CEAS Aeroacoustics Conference, Denver, 2017, https://doi.org/10.2514/6.2017-3004.
[5] B. Arnold, C. Rautmann, T. Lutz, E. Kraemer, Design of a boundary-layer suction system for trailing-edge noise reduction of an industrial wind turbine, in: 35th Wind Energy Symposium, Grapevine, 2017, https://doi.org/10.2514/6.2017-1380.
[6] A.L. Mardsen, M. Wang, J.E. Dennis, P. Moin, Trailing edge noise reduction using derivative-free optimization and large eddy simulation, J. Fluid Mech. 572 (2007) 13–36, https://doi.org/10.1017/S0022112006003235.
[7] S. Oerlemans, M. Fisher, T. Maeder, K. Kogler, Reduction of wind turbine noise using optimized airfoils and trailing-edge serrations, AIAA J. 47 (6) (2009) 1470–1481, https://doi.org/10.2514/1.38888.
[8] D.J. Moreau, C.J. Doolan, Noise-reduction mechanism of a flat-plate serrated trailing edge, AIAA J. 51 (10) (2013) 2513–2522, https://doi.org/10.2514/1.j052436.
[9] C. Arce León, D. Ragni, S. Pröbsting, F. Scarano, J. Madsen, Flow topology and acoustic emissions of trailing edge serrations at incidence, Exp. Fluid 57 (5) (2016) 1–17, https://doi.org/10.1007/s00348-016-2181-1.
[10] F. Avallone, S. Pröbsting, D. Ragni, Three-dimensional flow field over a trailing-edge serration and implications on broadband noise, Phys. Fluids 28 (11) (2016) 117101, https://doi.org/10.1063/1.4966633.
[11] I.A. Clark, W.N. Alexander, W. Devenport, S. Glegg, J.W. Jaworski, C. Daly, N. Peake, Bio-inspired trailing-edge noise control, AIAA J. 55 (3) (2017) 740–754, https://doi.org/10.2514/1.j055243.
[12] M. Herr, W. Dobrzynski, Experimental investigations in low-noise trailing edge design, AIAA J. 43 (6) (2005) 1167–1175, https://doi.org/10.2514/1.11101.
[13] A. Finez, M. Jacob, E. Jondeau, M. Roger, Broadband noise reduction with trailing edge brushes, in: 16th AIAA/CEAS Aeroacoustics Conference, Stockholm, 2010, https://doi.org/10.2514/6.2010-3980.
[14] R.R. Graham, The silent flight of owls, J. R. Aeronaut. Soc. 38 (286) (1934) 837–843, https://doi.org/10.1017/S0368393100109915.
[15] S. Lee, Reduction of blade-vortex interaction noise through porous leading edge, AIAA J. 32 (3) (1994) 480–488, https://doi.org/10.2514/3.12011.
[16] J. Revell, H. Kuntz, F. Balena, C. Horne, B. Storms, R. Dougherty, Trailing-edge flap noise reduction by porous acoustic treatment, in: 3rd AIAA/CEAS Aeroacoustics Conference, Atlanta, 1997, https://doi.org/10.2514/6.1997-1646.
[17] T. Sueki, T. Takaishi, M. Ikeda, N. Arai, Application of porous material to reduce aerodynamic sound from bluff bodies, Fluid Dynam. Res. 42 (1) (2010) 1–15, https://doi.org/10.1088/0169-5983/42/1/015004.
[18] S.A.S. Ali, M. Azarpeyvand, C.R.I. da Silva, Experimental study of porous treatment for aerodynamic and aeroacoustic purposes, in: 23rd AIAA/CEAS Aeroacoustics Conference, Denver, 2017, https://doi.org/10.2514/6.2017-3358.
[19] A. Vathylakis, T.P. Chong, P.F. Joseph, Poro-serrated trailing-edge devices for airfoil self-noise reduction, AIAA J. 53 (11) (2015) 3379–3394, https://doi.org/10.2514/1.j053983.
[20] T.P. Chong, E. Dubois, Optimization of the poro-serrated trailing edges for airfoil broadband noise reduction, J. Acoust. Soc. Am. 140 (2) (2016) 1361–1373, https://doi.org/10.1121/1.4961362.
[21] S. Oerlemans, Reduction of wind turbine noise using blade trailing edge devices, in: 22nd AIAA/CEAS Aeroacoustics Conference, Lyon, 2016, https://doi.org/10.2514/6.2016-3018.
[22] F. Avallone, W.C.P. van der Velden, D. Ragni, D. Casalino, Noise reduction mechanisms of sawtooth and combed-sawtooth trailing-edge serrations, J. Fluid Mech. 848 (2018) 560–591, https://doi.org/10.1017/jfm.2018.377.
[23] T. Geyer, E. Sarradj, Noise generation by porous airfoils, in: 13th AIAA/CEAS Aeroacoustics Conference, Rome, 2007, https://doi.org/10.2514/6.2007-3719.
[24] T. Geyer, E. Sarradj, C. Fritzsche, Porous airfoils: noise reduction and boundary layer effects, Int. J. Aeroacoustics 9 (6) (2010) 787–820, https://doi.org/10.1260/1475-472x.9.6.787.
[25] T. Geyer, E. Sarradj, Trailing edge noise of partially porous airfoils, in: 20th AIAA/CEAS Aeroacoustics Conference, Atlanta, 2014, https://doi.org/10.2514/6.2014-3039.
[26] M. Herr, K.S. Rossignol, J. Delfs, N. Lippitz, M. Moßner, Specification of porous materials for low-noise trailing-edge applications, in: 20th AIAA/CEAS Aeroacoustics Conference, Atlanta, 2014, https://doi.org/10.2514/6.2014-3041.
[27] M. Moßner, R. Radespiel, Modelling of turbulent flow over porous media using a volume averaging approach and a Reynolds stress model, Comput. Fluids 108 (2015) 25–42, https://doi.org/10.1016/j.compfluid.2014.11.024.
[28] J.E. Ffowcs-Williams, L.H. Hall, Aerodynamic sound generation by turbulent flow in the vicinity of a scattering half plane, J. Fluid Mech. 40 (4) (1970) 657–670, https://doi.org/10.1017/s0022112070000368.
[29] W.K. Blake, Mechanics of Flow-induced Sound and Vibration, vol. 2, Elsevier Science Publishing Co Inc, 2017.
[30] O. Stalnov, P. Chaitanya, P.F. Joseph, Towards a non-empirical trailing edge noise prediction model, J. Sound Vib. 372 (2016) 50–68, https://doi.org/10.1016/j.jsv.2015.10.011.
[31] W.A. Timmer, Two-dimensional low-Reynolds number wind tunnel results for airfoil NACA 0018, Wind Eng. 32 (6) (2008) 525–537, https://doi.org/10.1260/030952408787548848.
[32] F. Avallone, W.C.P. van der Velden, R. Merino-Martínez, D. Ragni, Near-wall pressure fluctuations over noise reduction add-ons, in: 23rd AIAA/CEAS Aeroacoustics Conference, Denver, 2017, https://doi.org/10.2514/6.2017-4171.
[33] F. Avallone, W.C.P. van der Velden, D. Ragni, Benefits of curved serrations on broadband trailing-edge noise reduction, J. Sound Vib. 400 (2017) 167–177, https://doi.org/10.1016/j.jsv.2017.04.007.
[34] C.A. Leon, F. Avallone, S. Pröbsting, D. Ragni, PIV investigation of the flow past solid and slitted sawtooth serrated trailing edges, in: 54th AIAA Aerospace Sciences Meeting, San Diego, 2016, https://doi.org/10.2514/6.2016-1014.
[35] C. Arce León, R. Merino-Martínez, D. Ragni, F. Avallone, M. Snellen, Boundary layer characterization and acoustic measurements of flow-aligned trailing edge serrations, Exp. Fluid 57 (12) (2016) 182, https://doi.org/10.1007/s00348-016-2272-z.
[36] M. Drela, XFOIL: an Analysis and Design System for Low Reynolds Number Airfoils, Springer Berlin Heidelberg, 1989, pp. 1–12, https://doi.org/10.1007/978-3-642-84010-4_1.
[37] S. F. J. Butler, Current Tests on Laminar-boundary-layer Control by Suction through Perforations, Aeronautical Research Council Reports and Memoranda 3040 (3040).
[38] J.H.M. Gooden, Experimental low-speed aerodynamic characteristics of the Wortmann FX66-S-196 V1 airfoil, in: XVI OSTIV Congress, Chateauroux, France, 1978.
[39] D. Lentink, R. de Kat, Gliding swifts attain laminar flow over rough wings, PLoS One 9 (6) (2014) e99901, https://doi.org/10.1371/journal.pone.0099901.
[40] S. Kim, C. Lee, A review on manufacturing and application of open-cell metal foam, Procedia Mater. Sci. 4 (2014) 305–309, https://doi.org/10.1016/j.mspro.2014.07.562.
[41] D. Ingham, I. Pop, Transport Phenomena in Porous Media, first ed., Pergamon, 1998.

[42] E. Baril, A. Mostafid, L.-P. Lefebvre, M. Medraj, Experimental demonstration of entrance/exit effects on the permeability measurements of porous materials, Adv. Eng. Mater. 10 (9) (2008) 889–894, https://doi.org/10.1002/adem.200800142.
[43] N. Dukhan, K. Patel, Effect of sample's length on flow properties of open-cell metal foam and pressure-drop correlations, J. Porous Mater. 18 (6) (2010) 655–665, https://doi.org/10.1007/s10934-010-9423-z.
[44] J. Despois, A. Mortensen, Permeability of open-pore microcellular materials, Acta Mater. 53 (5) (2005) 1381–1388, https://doi.org/10.1016/j.actamat.2004.11.031.
[45] J.P. Bonnet, F. Topin, L. Tadrist, Flow laws in metal foams: compressibility and pore size effects, Transport Porous Media 73 (2) (2007) 233–254, https://doi.org/10.1007/s11242-007-9169-5.
[46] T. Geyer, E. Sarradj, C. Fritzsche, Porous airfoils: noise reduction and boundary layer effects, in: 15th AIAA/CEAS Aeroacoustics Conference, Miami, 2009, https://doi.org/10.2514/6.2009-3392.
[47] T. Geyer, E. Sarradj, C. Fritzche, Measurement of the noise generation at the trailing edge of porous airfoils, Exp. Fluid 48 (291) (2010) 291–308, https://doi.org/10.1007/s00348-009-0739-x.
[48] G.I. Taylor, The spectrum of turbulence, Proc. R. Soc. A. 164 (919) (1938) 476–490, https://doi.org/10.1098/rspa.1938.0032.
[49] R.K. Amiet, Noise due to turbulent flow past a trailing edge, J. Sound Vib. 47 (3) (1976) 387–393, https://doi.org/10.1016/0022-460x(76)90948-2.
[50] R.K. Amiet, Acoustic radiation from an airfoil in a turbulent stream, J. Sound Vib. 41 (4) (1975) 407–420, https://doi.org/10.1016/s0022-460x(75)80105-2.
[51] R.K. Amiet, Effect of the incident surface pressure field on noise due to turbulent flow past a trailing edge, J. Sound Vib. 57 (2) (1978) 305–306, https://doi.org/10.1016/0022-460x(78)90588-6.
[52] R.R. Parchen, Progress Report DRAW: a Prediction Scheme for Trailing Edge Noise Based on Detailed Boundary Layer Characteristics, TNO report, TNO Institute of Applied Physics, 1998.
[53] F. Bertagnolio, A. Fischer, W.J. Zhu, Tuning of turbulent boundary layer anisotropy for improved surface pressure and trailing-edge noise modeling, J. Sound Vib. 333 (3) (2014) 991–1010, https://doi.org/10.1016/j.jsv.2013.10.008.
[54] A. Brandt, Noise and Vibration Analysis: Signal Analysis and Experimental Procedures, first ed., John Wiley & Sons, 2011, https://doi.org/10.1002/9780470978160.
[55] M. Kamruzzaman, T. Lutz, E. Kraemer, W. Wuerz, On the length scales of turbulence for aeroacoustic applications, in: 17th AIAA/CEAS Aeroacoustics Conference, Portland, 2011, https://doi.org/10.2514/6.2011-2734.
[56] G.P. Romano, Analysis of two-point velocity measurements in near-wall flows, Exp. Fluid 20 (2) (1995) 68–83, https://doi.org/10.1007/bf00189296.
[57] S. Luesutthiviboon, A. Malgoezar, M. Snellen, P. Sijtsma, D. Simons, Improving source discrimination performance by using an optimized acoustic array and adaptive high-resolution CLEAN-SC beamforming, in: 7th Berlin Beamforming Conference, Berlin, 2018.
[58] P. Sijtsma, R. Merino-Martinez, A.M.N. Malgoezar, M. Snellen, High-resolution CLEAN-SC: theory and experimental validation, Int. J. Aeroacoustics 16 (4–5) (2017) 274–298, https://doi.org/10.1177/1475472x17713034.
[59] L. Rayleigh, Investigations in optics, with special reference to the spectroscope, Phil. Mag. Series 8 (49) (1879) 261–274, https://doi.org/10.1080/14786447908639684 5.
[60] R. Merino-Martínez, M. Snellen, D.G. Simons, Functional beamforming applied to imaging of flyover noise on landing aircraft, J. Aircraft 53 (6) (2016) 1830–1843, https://doi.org/10.2514/1.c033691.
[61] T.J. Mueller, Aeroacoustic Measurements, Berlin New York Springer, 2002, https://doi.org/10.1007/978-3-662-05058-3.
[62] E. Sarradj, G. Herold, P. Sijtsma, R.M. Martinez, T.F. Geyer, C.J. Bahr, R. Porteous, D. Moreau, C.J. Doolan, A microphone array method benchmarking exercise using synthesized input data, in: 23rd AIAA/CEAS Aeroacoustics Conference, Denver, 2017, https://doi.org/10.2514/6.2017-3719.
[63] R. Merino-Martínez, W. van der Velden, F. Avallone, D. Ragni, Acoustic measurements of a DU96-W-180 airfoil with flow-misaligned serrations at a high Reynolds number in a closed-section wind tunnel, in: 7th International Conference on Wind Turbine Noise, Rotterdam, 2017.
[64] R. Merino-Martínez, P. Sijtsma, M. Snellen, Inverse integration method for distributed sound sources, in: 7th Berlin Beamforming Conference, Berlin, 2018.
[65] F. Scarano, M. Riethmuller, Advances in iterative multigrid PIV image processing, Exp. Fluid 29 (2000) 51–60, https://doi.org/10.1007/s003480070007.
[66] F. Scarano, Iterative image deformation methods in PIV, Meas. Sci. Technol. 13 (1) (2001) 1–19, https://doi.org/10.1088/0957-0233/13/1/201.
[67] J. Westerweel, F. Scarano, Universal outlier detection for PIV data, Exp. Fluid 39 (6) (2005) 1096–1100, https://doi.org/10.1007/s00348-005-0016-6.
[68] J. Westerweel, Fundamentals of digital particle image velocimetry, Meas. Sci. Technol. 8 (12) (1997) 1379–1392, https://doi.org/10.1088/0957-0233/8/12/002.
[69] M. Raffel, C.E. Willert, J. Kompenhans, Particle Image Velocimetry, third ed., Springer Berlin Heidelberg, 1998, https://doi.org/10.1007/978-3-662-03637-2.
[70] A. Melling, Tracer particles and seeding for particle image velocimetry, Meas. Sci. Technol. 8 (12) (1997) 1406–1416, https://doi.org/10.1088/0957-0233/8/12/005.
[71] R.J. Moffat, Describing the uncertainties in experimental results, Exp. Therm. Fluid Sci. 1 (1) (1988) 3–17, https://doi.org/10.1016/0894-1777(88)90043-x.
[72] B. Wieneke, PIV uncertainty quantification from correlation statistics, Meas. Sci. Technol. 26 (7) (2015) 074002, https://doi.org/10.1088/0957-0233/26/7/074002.
[73] F.F.J. Schrijer, F. Scarano, Effect of predictor–corrector filtering on the stability and spatial resolution of iterative PIV interrogation, Exp. Fluid 45 (5) (2008) 927–941, https://doi.org/10.1007/s00348-008-0511-7.
[74] A.R. Carpio, F. Avallone, D. Ragni, On the role of the flow permeability of metal foams on trailing edge noise reduction, in: 24th AIAA/CEAS Aeroacoustics Conference, Atlanta, 2018, https://doi.org/10.2514/6.2018-2964.
[75] B.C.J. Moore, Hearing, first ed., Academic Press, 1995.
[76] P.R. Spalart, J.H. Watmuff, Experimental and numerical study of a turbulent boundary layer with pressure gradients, J. Fluid Mech. 249 (1) (1993) 337–371, https://doi.org/10.1017/s002211209300120x.
[77] F.H. Clauser, The turbulent boundary layer, in: Advances in Applied Mechanics, Elsevier, 1956, pp. 1–51, https://doi.org/10.1016/s0065-2156(08)70370-3.
[78] P. Krogstad, R.A. Antonia, L.W.B. Browne, Comparison between rough- and smooth-wall turbulent boundary layers, J. Fluid Mech. 245 (1) (1992) 599–617, https://doi.org/10.1017/s0022112092000594.
[79] K.A. Flack, M.P. Schultz, Roughness effects on wall-bounded turbulent flows, Phys. Fluids 26 (10) (2014) 101305, https://doi.org/10.1063/1.4896280.
[80] S.A.S. Ali, M. Azarpeyvand, C.R.I. da Silva, Trailing-edge flow and noise control using porous treatments, J. Fluid Mech. 850 (2018) 83–119, https://doi.org/10.1017/jfm.2018.430.
[81] M. Moßner, R. Radespiel, Flow simulations over porous media: comparisons with experiments, Comput. Fluids 154 (2017) 358–370, https://doi.org/10.1016/j.compfluid.2017.03.002.
[82] Y. Kametani, K. Fukagata, R. Örlü, P. Schlatter, Effect of uniform blowing/suction in a turbulent boundary layer at moderate Reynolds number, Int. J. Heat Fluid Flow 55 (2015) 132–142, https://doi.org/10.1016/j.ijheatfluidflow.2015.05.019.
[83] A. Bodling, B.R. Agrawal, A. Sharma, I. Clark, W.N. Alexander, W.J. Devenport, Numerical investigation of bio-inspired blade designs at high Reynolds numbers for ultra-quiet aircraft and wind turbines, in: 23rd AIAA/CEAS Aeroacoustics Conference, Denver, 2017, https://doi.org/10.2514/6.2017-3502.
[84] S. Glegg, W. Devenport, The far-field sound from rough-wall boundary layers, Proc. R. Soc. A. 465 (2106) (2009) 1717–1734, https://doi.org/10.1098/rspa.2008.0318.
[85] C. Tropea, A. Yarin, J.F. Foss (Eds.), Handbook of Experimental Fluid Mechanics, first ed., Springer, 2016.
[86] A. Garcia-Sagrado, T. Hynes, Wall pressure sources near an airfoil trailing edge under turbulent boundary layers, J. Fluid Struct. 30 (2012) 3–34, https://doi.org/10.1016/j.jfluidstructs.2011.12.007.
[87] J.M. Wallace, H. Eckelmann, R.S. Brodkey, The wall region in turbulent shear flow, J. Fluid Mech. 54 (01) (1972) 39–48, https://doi.org/10.1017/s0022112072000515.
[88] J.M. Wallace, Quadrant analysis in turbulence research: history and evolution, Annu. Rev. Fluid Mech. 48 (1) (2016) 131–158, https://doi.org/10.1146/annurev-fluid-122414-034550.

[89] S. Ghaemi, F. Scarano, Turbulent structure of high-amplitude pressure peaks within the turbulent boundary layer, J. Fluid Mech. 735 (2013) 381–426, https://doi.org/10.1017/jfm.2013.501.
[90] T.P. Chong, A. Vathylakis, On the aeroacoustic and flow structures developed on a flat plate with a serrated sawtooth trailing edge, J. Sound Vib. 354 (2015) 65–90, https://doi.org/10.1016/j.jsv.2015.05.019.
[91] W.W. Willmarth, S.S. Lu, Structure of the Reynolds stress near the wall, J. Fluid Mech. 55 (1) (1972) 65–92, https://doi.org/10.1017/s002211207200165x.
[92] M.R. Raupach, Conditional statistics of Reynolds stress in rough-wall and smooth-wall turbulent boundary layers, J. Fluid Mech. 108 (1981) 363–382, https://doi.org/10.1017/s0022112081002164.
[93] K. Suga, M. Mori, M. Kaneda, Vortex structure of turbulence over permeable walls, Int. J. Heat Fluid Flow 32 (3) (2011) 586–595, https://doi.org/10.1016/j.ijheatfluidflow.2011.02.016.
[94] A. Kolmogorov, The local structure of turbulence in incompressible viscous fluid for very large Reynolds numbers, Dokl. Akad. Nauk SSSR 30 (1941) 301–305.
[95] D.T. Squire, N. Hutchins, C. Morrill-Winter, M.P. Schultz, J.C. Klewicki, I. Marusic, Applicability of taylor's hypothesis in rough- and smooth-wall boundary layers, J. Fluid Mech. 812 (2016) 398–417, https://doi.org/10.1017/jfm.2016.832.
[96] M. Kamruzzaman, T. Lutz, A. Ivanov, A. Herrig, W. Wuerz, E. Kraemer, Evaluation of measured anisotropic turbulent two-point correlation data for the accurate prediction of the turbulence noise sources, in: 15th AIAA/CEAS Aeroacoustics Conference, Miami, 2009, https://doi.org/10.2514/6.2009-3313.
[97] S.B. Pope, Turbulent Flows, first ed., Cambridge University Press, 2000.